Universidade de Aveiro Departamento de Física
Ano 2016/2017

Bohdan Kulyk

Grafeno CVD para Biodeteção Eletroquímica: Síntese, Caracterização e Desenvolvimento de Dispositivos

CVD Graphene for Electrochemical Biosensing: Synthesis, Characterisation and Device Fabrication

Universidade de Aveiro Departamento de Física
Ano 2016/2017

Bohdan Kulyk

Grafeno CVD para Biodeteção Eletroquímica: Síntese, Caracterização e Desenvolvimento de Dispositivos

CVD Graphene for Electrochemical Biosensing: Synthesis, Characterisation and Device Fabrication

Dissertação apresentada à Universidade de Aveiro para cumprimento dos requisitos necessários à obtenção do grau de Mestre em Engenharia Física, realizada sob a orientação científica da Doutora Florinda Mendes da Costa, professora associada do Departamento de Física da Universidade de Aveiro, do Dr. António José Silva Fernandes, técnico superior do Departamento de Física da Universidade de Aveiro e da Doutora Sónia Oliveira Pereira, estagiária de pós-doutoramento do Departamento de Física da Universidade de Aveiro.

Apoio financeiro do FEDER através do programa COMPETE 2020 e da FCT – Fundação portuguesa para a Ciência e Tecnologia através dos projetos UID/CTM/50025/2013.

Dedicado aos meus pais e à minha avó, que tanto fizeram para me verem chegar aqui.

o júri

presidente	Prof. Doutor António Ferreira da Cunha professor auxiliar do Departamento de Física da Universidade de Aveiro
orientadora	Prof.ª Doutora Florinda Mendes da Costa professora associada do Departamento de Física da Universidade de Aveiro
arguente	Prof.ª Doutora Maria Goreti Ferreira Sales professora adjunta do Departamento de Engenharia Química do Instituto Superior de Engenharia do Porto

agradecimentos

Gostaria de começar por agradecer à Professora Doutora Florinda da Costa e ao Dr. António José Fernandes não só pela orientação científica que deram, mas também pelo esforço e preocupação que sempre demonstraram no sentido de proporcionar um local de trabalho amigável e acolhedor, algo que valorizo bastante.

Agradeço também à Doutora Sónia Oliveira por ter acompanhado tão de perto o meu trabalho e por ter contribuído tanto para o mesmo.

Obrigado também ao Nuno Santos pela experiência que partilhou, algo que foi essencial para ultrapassar algumas das maiores dificuldades enfrentadas neste trabalho.

Ao Alexandre, um muito obrigado pelas discussões, pela partilha de ideias e pela ajuda nas diversas fases de trabalho. Mas acima de tudo, obrigado pelo exemplo dado que tanto me motivou ao longo dos últimos anos.

Não posso também deixar de agradecer ao Filipe Martinho, com quem aprendi muito não só ao longo de inúmeros trabalhos e discussões, mas também pela sua forma de ser no contexto académico e científico.

Por fim, agradeço a todos os meus colegas e amigos mais próximos, bem como à minha família.

palavras-chave

Grafeno, Deposição Química em Fase Vapor, Biossensor, Funcionalização, Espetroscopia de Impedância Eletroquímica.

resumo

O presente trabalho descreve o desenvolvimento de um biossensor onde o grafeno desempenha o papel do elemento transdutor. A revisão da literatura relativamente ao enquadramento do grafeno na área da biodeteção revelou a espetroscopia de impedância eletroquímica (EIS) como uma técnica de deteção viável.

As amostras de grafeno foram sintetizadas em substratos de cobre, por deposição química em fase vapor, tendo sido posteriormente caracterizadas por espetroscopia de Raman, microscopia eletrónica de varrimento (SEM), microscopia ótica, EIS e voltametria de pulso diferencial (DPV). O processo de transferência do grafeno para substratos de Si/SiO_2 foi otimizado de modo a preservar a qualidade das amostras e melhorar a sua reprodutibilidade.

Para a modificação da superfície de grafeno necessária ao mecanismo de deteção, foram exploradas as abordagens de funcionalização covalente e não-covalente. Esta última, baseada na ligação dos elementos de bioreconhecimento (biotina e anti-gonadotrofina coriónica humana, hCG) aos grupos amina de pyrene butyric hydrazide (PBH) imobilizada na superfície do grafeno, foi estudada usando a espetroscopia de Raman, espetroscopia de fotoeletrões excitados por raios-X (XPS) e EIS.

Por fim, os testes de deteção foram realizados através da avaliação das alterações nos espetros de EIS em resposta às diferentes concentrações do analito (avidina ou hCG).

As amostras sintetizadas foram identificadas como sendo grafeno monocamada com ilhas de poucas camadas e mostraram uma atividade eletroquímica reduzida. Relativamente às estratégias de funcionalização, a covalente não foi bem-sucedida, ao contrário da não-covalente. Contudo, os esforços no sentido da otimização deste processo não foram suficientes para que se conseguisse atingir uma conclusão clara acerca da concentração ideal de PBH. As amostras biofuncionalizadas mostraram uma resposta inconclusiva face às diferentes concentrações do analito testadas.

keywords

Graphene, Chemical Vapour Deposition, Biosensor, Functionalisation, Electrochemical Impedance Spectroscopy.

abstract

This work describes the efforts undertaken towards the development of a biosensing device with graphene as a transducing element. A literature review was conducted in order to establish graphene's role in the biosensing field, with electrochemical impedance measurements having been identified as a viable sensing approach.

The graphene samples were synthesised by thermal chemical vapour deposition (TCVD) on Cu substrates and characterised using Raman spectroscopy, Scanning Electron Microscopy (SEM), optical microscopy, Electrochemical Impedance Spectroscopy (EIS) and Differential Pulse Voltammetry (DPV). Also, the transfer of the as-grown samples onto Si/SiO_2 substrates was optimised.

A functionalisation stage followed, with both covalent and non-covalent approaches having been explored. The latter, based on the attachment of the biorecognition elements (biotin and anti-human Chorionic Gonadotropin, hCG) to the amine groups of pyrene butyric hydrazide (PBH) immobilized on graphene's surface, was studied using Raman spectroscopy, X-ray Photoelectron Spectroscopy (XPS) and EIS.

Lastly, sensing tests were conducted by evaluating the changes in EIS spectra in response to different concentrations of the analyte (either avidin or hCG).

The as-grown samples were identified as being single-layer graphene with few-layer islands and showed reduced electrochemical activity. Concerning the functionalisation strategies, the covalent one was unsuccessful, while the non-covalent one was achieved. However, the efforts towards the optimisation of this process were not enough to reach a clear conclusion regarding the optimal concentration of PBH. The biofunctionalised samples did not show a clear response to the different analyte concentrations.

Contents

List of Figures

List of Tables

Abbreviations

APTES	3-Aminopropyl-triethoxysilane
BSA	Bovine Serum Albumin
DMF	N,N-dimethylformamide
DPV	Differential Pulse Voltammetry
EDC	N-(3-dimethylaminopropyl)-N'-ethylcarbodiimide hydrochlorine
EIS	Electrochemical Impedance Spectroscopy
EDS	Energy Dispersive X-ray Spectroscopy
hCG	Human Chorionic Gonadotropin
IPA	Isopropyl alcohol
LOD	Limit of Detection
LOQ	Limit of Quantitation
NHS	N-hydroxysuccinimide
PBH	Pyrene Butyric Hydrazide
PBS	Phosphate Buffer Saline
PMMA	(poly(methyl methacrylate))
SEM	Scanning Electron Microscopy
TCVD	Thermal Chemical Vapour Deposition
XPS	X-ray Photoelectron Spectroscopy

1. Introduction

It was in 1947 that graphene, a two-dimensional layer of carbon atoms arranged in a honeycomb pattern, was described by P. R. Wallace [1]. This description, however, presented graphene not as a distinct allotrope of carbon, like diamond or graphite, but rather as a concept describing a single sheet of the latter, useful for the theoretical description of graphite's electrical properties. Even after other carbon-based materials have been discovered, such as carbon nanotubes [2] and fullerenes [3], graphene continued to be thought of as most likely unstable as an isolated allotrope [4], and, at best, as an unremarkable building block of regular graphite.

The perception of graphene changed when, in 2004, A. K. Geim and K. S. Novoselov were able to isolate a single layer of this atomically thin material by a repeated peeling of small mesas of highly-oriented pyrolytic graphite (HOPG), using nothing more than a mere piece of scotch tape [5]. More importantly, they demonstrated, by using graphene as a conductive channel in a field-effect transistor (FET), that it possessed excellent electrical properties, far better than those of graphite. Soon after, reports of graphene's outstanding mechanical, optical and thermal properties attracted even more attention from the scientific community. As a result, the number of published works on graphene skyrocketed (see Figure 1) and, in 2010, Geim and Novoselov were awarded the Nobel Prize in Physics.

Currently, the interest in graphene is far beyond purely academic. Even on their own, some of graphene's superior qualities point in the direction of improved products and devices, such as faster electronics [6] and stronger composites [7], among many others. Moreover, by simultaneously taking advantage of several of these outstanding properties, graphene justifies the attention given to it, by opening the door towards entirely new applications and technological concepts. One

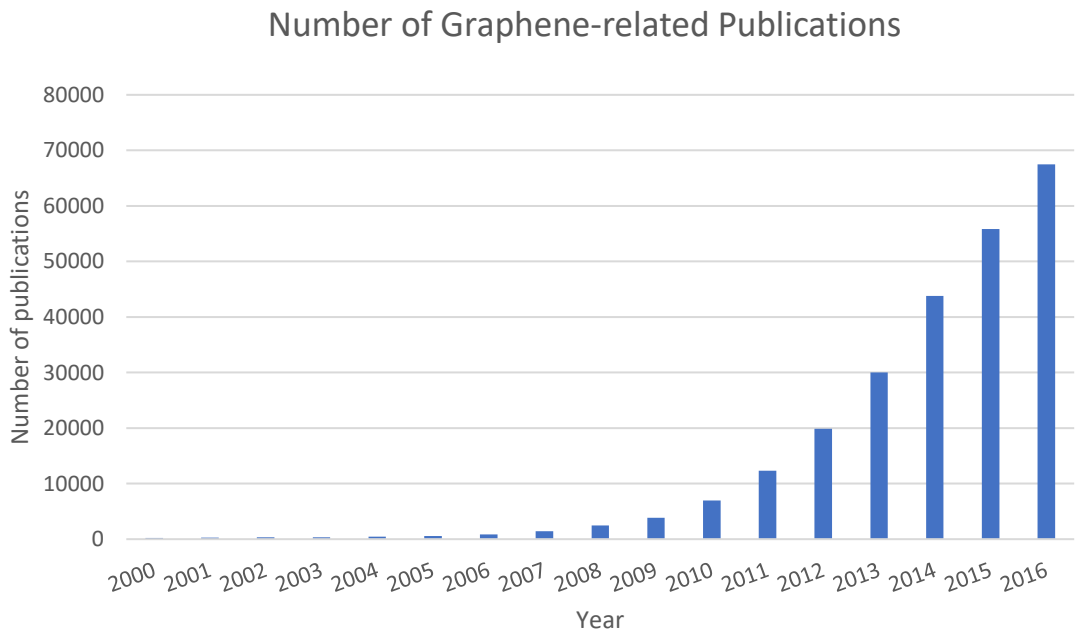

Figure 1 – Number of scientific publications with the word "Graphene" in the title, abstract or keywords, according to the Scopus online database.

example of this is the potential use of graphene as a transparent electrode in flexible handheld devices [8],[9], which would require a combination of good electrical conductivity, high optical transparency and flexibility. It was these and other potential applications of graphene that warranted an investment of 1 billion euros by the European Union, underlining the possibilities offered by this material [10].

Among a large number of fields where graphene has popped up in one capacity or another, one of the most exciting is that of biomedicine [11]. By taking advantage of graphene's chemical purity and large surface area, it can be used as a drug delivery vehicle [12], addressing issues related to drug loading capacity, thanks to its high-surface area. In the domain of regenerative medicine, graphene's mechanical properties can be useful in tissue engineering [13]. But perhaps more importantly, the electrical properties of this material, aided by its large surface area, allow the development of highly sensitive biosensors [14]–[16]. Reports of graphene-based biosensors for the detection of viruses [17], nucleic acids [18], antigens [19] and hormone biomarkers [20] have already demonstrated graphene's potential for improved diagnosis and health monitoring.

Nonetheless, and despite the promise graphene holds and the progress that has been made towards its large-scale application in biosensing devices, some challenges remain. In particular, the preparation of high quality graphene at an acceptable cost is an important stepping-stone for its further use (this challenge extends to other fields where graphene might be applied). Another difficulty arises with the need for high selectivity in such biosensors. This requires modification of the graphene surface through functionalisation [21], which can be detrimental to its electrical properties. Thus, controllable, reproducible and stable functionalisation techniques are necessary.

This work covers the entire development process of a graphene-based biosensor, from graphene synthesis to the observation of biosensing behaviour. More specifically, single-layer graphene with few-layer islands, grown by chemical vapour deposition, a cheap and simple growth technique, is developed and characterized. Subsequently, the functionalisation of the graphene films is explored, both through covalent and non-covalent strategies. Here, the non-covalent one reveals to be more successful as pyrene butyric hydrazide (PBH) acts as a linker between graphene and a target-specific protein or antibody (biotin and anti-human chorionic gonadotropin, respectively). An effort towards the optimisation of the functionalisation process is undertaken. Finally, the biosensing behaviour of the modified samples is demonstrated by establishing a relationship between the charge transfer resistance, R_{ct}, of the sensors, extracted from the fitting of the measured electrochemical impedance spectra, and the concentration of the chosen analytes (avidin and human Chorionic Gonadotropin).

1.1. Graphene

1.1.1. Structure and Properties

Graphene is a single-atom-thick sheet of sp^2-bonded carbon atoms, arranged in a honeycomb pattern, which is either freely suspended or adhered to a foreign substrate [22]. The stacking of individual graphene sheets leads to materials known as bilayer, trilayer, few-layer and multilayer graphenes, depending on the number of sheets.

The two-dimensional (2D) lattice of monolayer graphene is formed by two interpenetrating planar triangular lattices, with a relative shift of $a = 142\ pm$ [24, pg. 601] (Figure 2 (a)). It is worth noting that two-dimensional structures were thought to be unstable [4]. However, the intrinsic rippling of the graphene sheet might be responsible for its natural occurrence as a planar structure [24]. The reciprocal lattice of graphene presents a similar honeycomb pattern, giving rise to a hexagonal 1st Brillouin zone whose high symmetry points are marked in Figure 2 (b).

The lattice sites A and B are occupied by carbon atoms bonded by sp^2-hybridized bonds. Additionally, π bonding gives rise to delocalized electrons in graphene. But perhaps more importantly, the sublattices A and B allow for quantum mechanical hopping of electrons between the two, which in turn leads to two conically-shaped energy bands that intersect at the corners of the 1st Brillouin zone (Figure 3) [25]. These energy bands are known as Dirac cones and originate, for low energies, a linear dispersion relation $E = \hbar k v_F$, which is reminiscent of massless relativistic particles (where $\hbar$ is the reduced Plank constant and k the electron momentum) [26]. Here, the role of speed of light is played by the Fermi velocity, $v_F \approx 10^6\ m\ s^{-1}$. Because of this unique energy dispersion relation, several interesting quantum electrodynamics effects are present in graphene. One such example is the possibility of ballistic transport for distances of the order of magnitude of micrometers, resulting in electron mobilities as high as $\approx 200\,000\ cm^2\ V^{-1}\ s^{-1}$ [27]. Others include the anomalous Integer Quantum Hall Effect [28] and the Klein paradox [29]. Additionally, the absence of an electronic band-gap in graphene allows for an ambipolar electric field-effect, where charge carriers' density can be tuned by the application of a gate voltage in field-effect transistor (FET) devices with graphene as the conducting channel [5]. One of the shortcomings of such FETs (commonly referred to as GFETs), very attractive for high speed electronics [30], [31], would be their low on-off ratio (which precludes the existence of two clearly distinct states for logical operations), due to the absence of a band-gap in pristine graphene. However, an energy gap can be opened through interactions with a substrate [32] or by means of lateral confinement in graphene nano-ribbons [33], among other promising strategies [32], [34].

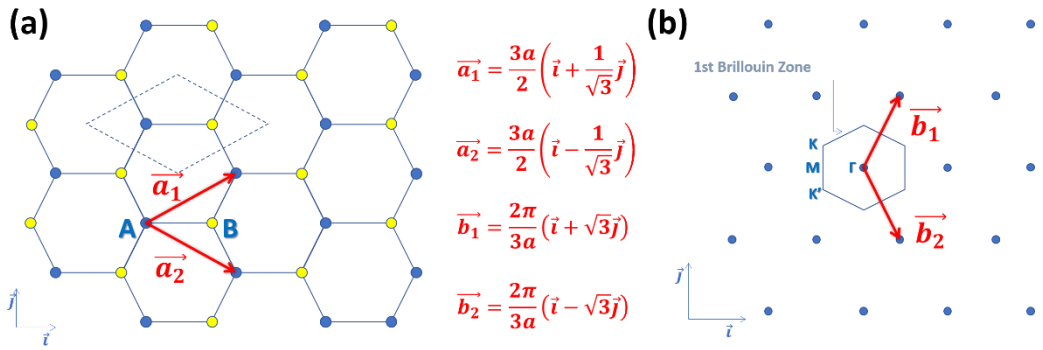

*Figure 2 – Graphene's atomic structure in **(a)** real and **(b)** reciprocal space, along with the respective unit vectors.*

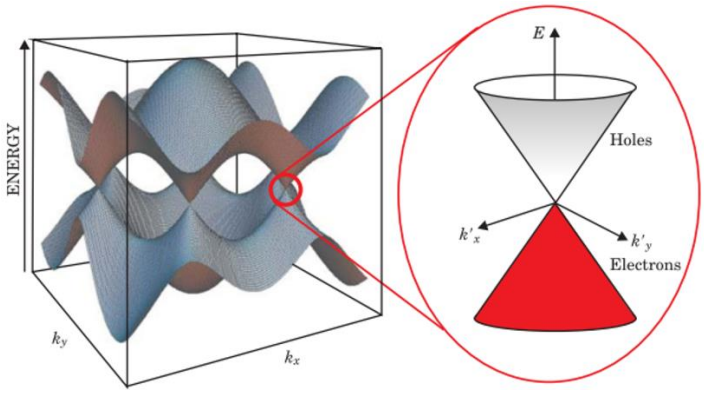

Figure 3 – Graphene's electronic band structure, highlighting the Dirac cones at the 1st Brillouin zone corners (points K and K'). Adapted from [35].

Graphene's optical properties are also of great interest to both fundamental science and engineering. A nearly constant optical transparency of 97.7% across the entire visible spectral region is a unique characteristic of this atom-thick material, thanks to its electronic band structure and dimensionality [36]. This, combined with graphene's electronic properties, paves the way for a new generation of devices in which graphene replaces the expensive, scarce and brittle indium tin oxide (ITO) as the transparent electrode [37]. Other optical properties of the material include nonlinear responses [38] such as high-harmonic generation, with harmonics as high as 9th having been obtained by mid-infrared laser pulse excitation [39].

Another aspect where graphene excels has to do with its mechanical properties. A Young's modulus of $E = 1.0\,TPa$ and intrinsic tensile strength of $\sigma_{int} = 130\,GPa$ are some of the highest ever reported for any known material [40]. Once again, it is the combination of graphene's outstanding properties, such as its flexibility, mechanical strength and good electronic properties, that make it highly desirable for applications such as micro- and nano-electromechanical systems (MEMS and NEMS) [41], flexible conductors [42] and conductive composites [43].

Superior thermal properties are another attribute of this carbon-based material. A thermal conductivity of up to $K = 5.30{\times}10^3\ W\ m^{-1}\ K^{-1}$ [44] is one of the highest known for any material. Furthermore, graphene's two-dimensional nature affords it some unique features of heat conduction. Specifically, the thermal conductivity of 2D materials is predicted to diverge as their size increases [45]. In practice, however, K is limited by such factors as the presence of defects and substrate coupling, among others [46]. Nonetheless, the excellent values of thermal conductivity make graphene a good prospect for thermal management applications [47].

1.1.2. Applications

The wide range of graphene's attractive properties makes it a prime candidate for a vast number of applications. The different fields where this material can acquire a relevant role were extensively reviewed by Ferrari *et al.* in the seminal "Science and technology roadmap for graphene, related two-dimensional crystals, and hybrid systems" [11]. The authors underline graphene's potential not just for improvement of current technologies, but also for its role in the emergence of entirely new, disruptive innovations. This is justified by the unprecedented combination of outstanding properties encountered in graphene.

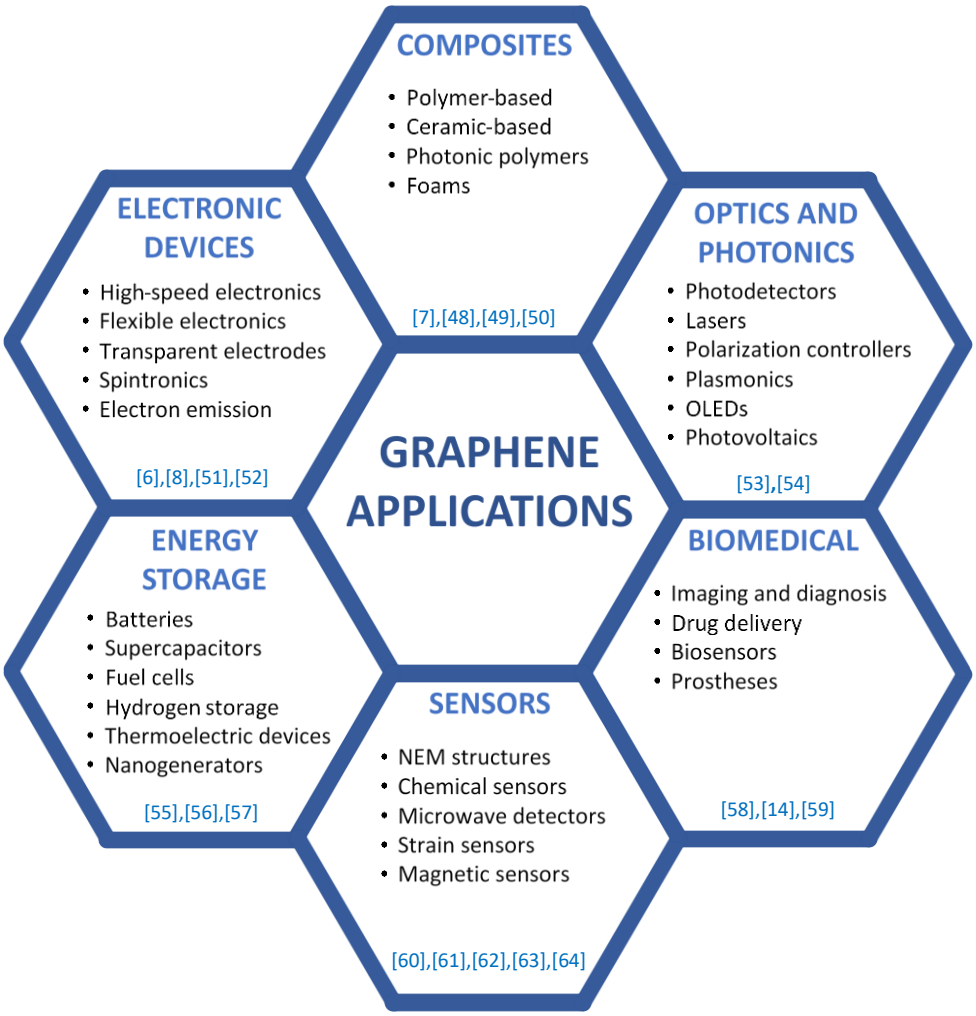

Figure 4 – Schematic summary of graphene's possible applications (devices and fields).

Given the sheer scale of graphene's potential, a review of all the possible applications of this material is well beyond the scope of the present work. Nonetheless, Figure 4 seeks to sum up the main areas and devices where graphene is expected to have an impact.

1.1.3. Characterisation

Several different techniques are commonly used to characterize graphene. Among these are optical microscopy [65], Scanning Electron Microscopy (SEM) [66], Transmission Electron Microscopy (TEM) [67], and Atomic Force Microscopy (AFM) [68]. However, none of these have the same relevance as Raman spectroscopy.

Raman spectroscopy relies on the analysis of the energy shift of photons due to Raman scattering that occurs when they interact with the sample [69]. By focusing a laser beam of a known wavelength on the sample and by analysing the energy of the scattered light, it is possible to identify its vibrational states. This gives information regarding the structure and composition of the sample.

The relevance of Raman spectroscopy for the characterisation of graphene, as pointed out by *A. Ferrari et al.* [70], is justified not only by graphene's unique Raman spectrum, but also by the information it provides regarding the material's structure, morphology and electronic properties,

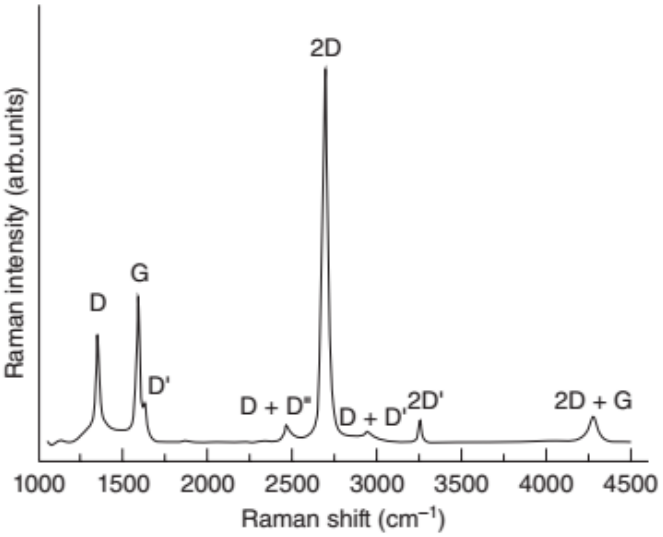

Figure 5 – Raman spectrum of monolayer graphene. [71].

among others. The simplicity and the non-destructive character of this technique strengthen its position of importance as a characterisation technique for graphene.

Looking at a typical Raman spectrum of graphene (Figure 5), one can identify several sharp peaks (also referred to as bands). The one appearing at $\sim 1580\ cm^{-1}$ (for $514\ nm$ excitation wavelength) is known as the G band and is originated by the stretching of the sp^2 carbon bonds (thus being present in all the allotropes in which the carbon bonds are sp^2 hybridized, such as graphite and carbon nanotubes) [72].

Another peak can be seen at $\sim 2700\ cm^{-1}$ (for $514\ nm$ excitation wavelength). This one, known as the 2D band, is due to the scattering of photo-excited electrons by two phonons of the breathing mode of the aromatic rings, by means of a double resonance mechanism [70]. The peak originated by the scattering by just one of these phonons is the D band and it appears at half the Raman shift of the 2D band ($\sim 1350\ cm^{-1}$, for $514\ nm$ excitation wavelength[1]). Note that unlike the 2D band, where the two phonons involved have symmetric momenta, the D band is not allowed for a perfect graphene lattice by the Raman fundamental selection rule that requires the sum of the wave vectors of the phonons to be zero, $q = 0$. However, for imperfect aromatic rings, such as the ones with defects or the ones at the graphene's edges (which can be seen as extended defects), these rules are relaxed and an additional scattering at the defect allows the appearance of the D band. Thus, the peak at $\sim 1350\ cm^{-1}$ is often used to identify the presence of defects in a graphene sample and to get a quantitative measure of said defects through the ratio of intensities of the D and G band, $I(D)/I(G)$ [74].

As for the 2D band, its importance comes from the possibility that it offers to identify the number of layers present in a graphene sample (up to 5 layers) [70]. For a single layer sample, the 2D band appears as a single, sharp peak, up to four times as intense as the G band [72]. For samples with more than one layer, the 2D band splits into four less intense peaks. This splitting is originated by the interaction between the different graphene planes, which causes the electronic bands to split

[1]The D band is dispersive with excitation energy, due to a Kohn anomaly at the K point of the first Brillouin zone, upshifting linearly with a slope of $50\ cm^{-1}/eV$ [73]. The dispersion of the 2D band is about twice as large [71].

into four bands [70]. For samples with more than five layers, the Raman spectra are nearly indistinguishable from those of graphite. It is worth pointing out, however, that the interaction between the graphene planes that leads to the electronic bands' splitting (and, consequently, to the splitting of the 2D band) only occurs for samples with Bernal (AB) stacking [71]. The 2D band in samples with multiple randomly oriented layers mimics the sharp 2D peak of monolayer graphene, accompanied by a small ($20\ cm^{-1}$ for $514\ nm$ excitation wavelength) upshift in its position and a broadening of its FWHM to $40 - 45\ cm^{-1}$. As the number of misoriented layers increases, the intensity of the 2D band has also been shown to decrease [75]. Thus, the ratio of the intensities of the 2D and G bands is often used to identify the possible presence of multiple layers in a graphene sample.

Another band typically described by a scattering process similar to that of the D band appears at $\sim 1620\ cm^{-1}$ [72]. This band, designated as D', is also associated with defects, due to the violation of the $q = 0$ selection rule. Its second order band appears at $\sim 3250\ cm^{-1}$ and is known as the 2D' band.

Other prominent bands in the graphene Raman spectrum are the D+D'' band, around $2450\ cm^{-1}$ ($532\ nm$ excitation wavelength), the D+D' band, at $2970\ cm^{-1}$ ($514\ nm$ excitation wavelength) and the 2D+G band at $4280\ cm^{-1}$ ($514\ nm$ excitation wavelength).

1.2. Biosensors and graphene's promise

1.2.1. General concepts in biosensing and device categorisation

A biosensor is a device that transforms a biochemical stimulus into an analytically useful signal through a biochemical recognition mechanism [76], [77]. The emergence of such devices can be traced back to the work of Leland C. Clark Jr. and Champ Lyons, who, in the early 60s, reported an electrochemical system for continuous recording of blood chemistry parameters and, in particular, of glucose concentration [78]. Currently, biosensors are being applied in a wide range of industrial, medical and scientific fields [79], with glucose biosensors themselves accounting for approximately 85% of biosensors' world market [80].

The basic structure of a biosensing device (Figure 6) is comprised by (1) a recognition component which differentiates the analyte from other (bio)chemicals in its environment, (2) a transducer that gives rise to a measurable signal in response to the analyte and (3) a processing module which translates the received signal into easily accessible information [76]. Different implementations of this general structure have been developed since Lyons and Clark's work.

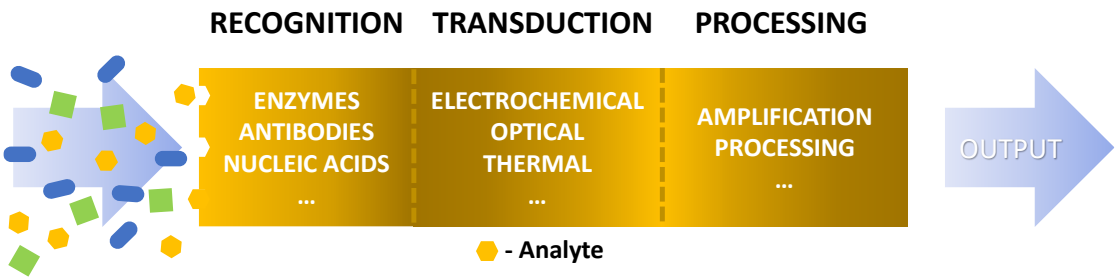

Figure 6 – Basic structure of a biosensor.

With regards to recognition components, several classes of biosensors can be identified [77]:

- **Biocatalytic recognition** – a chemical reaction is catalysed by a component incorporated into the biosensor. Different types of catalytic components are possible, such as enzymes, cells or cells' components, and tissues. The detection itself is then accomplished by monitoring one or several reaction dependent parameters. The most common example of such biosensors is a glucose biosensor. Here, the immobilized glucose oxidase (GOx) catalyses the oxidation of β-D-glucose [81]. This reaction produces gluconic acid and hydrogen peroxide (H_2O_2). The reaction parameters that can be measured in such a reaction, giving information on glucose concentration, are oxygen consumption, hydrogen peroxide production and electron transfer from GOx to an electrode, by means of a mediator. In hydrogen peroxide measurement, for example, the H_2O_2 molecule itself is oxidized at an electrode and the resulting current is measured and translated into a value for glucose concentration.
- **Biocomplexing or bioaffinity recognition** – a direct interaction, such as bonding, occurs between the receptor and the analyte. Typically, this type of interaction is of an immunochemical nature, whereas an antigen binds to a specific antibody. Alternatively, other ligands, such as aptamers (nucleic acid ligands like RNA, ssDNA, etc.) or proteins such as lectins [82], can be used. Usually, in this type of sensors equilibrium is reached once the binding is completed, and regeneration (forced dissociation of the bonds) is required to reuse the device. If regeneration is impossible, the biosensor must be discarded. To avoid non-specific binding (the binding of molecules other than the analyte), the surface of the biosensor can be passivated with a blocking agent, such as bovine serum albumin (BSA) or salmon sperm DNA [83].

As for the transducers, the exploitation of different mechanisms and effects leads to the following classification:

- **Magnetic biosensors** – effects such as giant magnetoresistance (GMR) [84], Hall effect [85] and superconducting quantum interference [86] are explored in order to translate chemical information into an easily measurable signal. Magnetic nanoparticles may be used, either through direct integration into the biosensor or through dispersion in the sample to be analysed, allowing simultaneous multi-analyte detection [87], [88].
- **Optical biosensors** – changes in the response of the recognition component to the optical field are used to identify and quantify the presence of an analyte. Surface plasmon resonance, evanescent wave fluorescence, luminescence and surface-enhanced Raman scattering, among other phenomena, are exploited in this type of sensors [89].
- **Piezoelectric biosensors** – typically built in the form of what is known as a Piezoelectric Quartz Microbalance, a piezoelectric crystal coated with a selective biocomponent that binds to the analyte is placed between two electrodes to which an AC voltage is applied. This voltage forces the crystal to vibrate at a specific resonance frequency, which is altered by the binding of the analyte to the crystal's surface in response to the change in the device's mass [90].
- **Thermometric (or calorimetric) biosensors –** a chemical reaction involving the analyte is catalysed and the change in the temperature within the reaction medium due to either absorption or release of heat by said reaction is measured [91].
- **Electrochemical biosensors –** a chemically modified electrode is used as a transducer, directly translating an interaction with the analyte (be it a reaction or a binding event) into

an electrical signal [77]. This is by far the most common type of transducing mechanism, thanks to its widespread use in glucose biosensors [92].

It is the latter class of devices, the electrochemical biosensors, that will be explored in this work. A brief overview of the different modes of operation of such devices, along with a basic description of the underlying physics is given below.

Amperometic devices

An amperometric electrochemical biosensor is based on the measurement of the current signal that arises as the device interacts with the analyte through a reduction or an oxidation reaction. Typically, three electrodes separated by an electrolyte are used: a working-electrode, where the sensing occurs, a reference-electrode, held at a known, constant potential, and a counter-electrode, which completes the circuit in a setup known as the electrochemical cell [76]. A potential (either constant or varying) is applied to the working-electrode relative to the reference-electrode [77]. In the case of a constant potential (a technique called amperometry [76]), it is chosen so that the current depends on the number of electrons involved in the reaction, n, the electrode area, A, the Faraday constant, $F = 96485.33289\ C\ mol^{-1}$, and the flux of the analyte at the interfacial boundary, j. The flux of the analyte describes the reaction rate and is given by the product of the heterogeneous electron transfer rate constant, k, and the concentration of the analyte at the working electrode/electrolyte interface, C. Thus, the measured current can be written as [92]:

$$i = nFAkC \tag{1}$$

As can be seen from Eq. (1), the current i is directly proportional to the analyte's concentration C, which allows such a setup to function as a sensor. Alternatively, the current can be registered as the potential is swept in a specific manner. This technique is known as voltammetry. Cyclic voltammetry, differential pulse voltammetry or square wave voltammetry are some of the measurement methods used in amperometric biosensors.

The most common example of amperometric devices is the glucose biosensor [76], [92]. Recognition elements other than the biocatalytic ones can also be used in amperometric devices, as exemplified by the amperometric immunosensor reported by Santandreu *et al.* [93].

Potentiometric Devices

In potentiometric devices, which also use the three-electrode setup, there is no current flowing through the working electrode. Instead, it is the potential built-up due to the accumulation of ionic charge at an interface that is measured. This potential, E, can be related to the ion activity, a_I, through the Nernst equation [94]:

$$E = E^0 + \frac{RT}{zF} \ln a_I, \tag{2}$$

where E^0 is a constant potential contribution, R is the universal gas constant, T is the absolute temperature and z is the ion's charge. It is worth pointing out that a_I describes the concentration of uncomplexed analyte. For dilute solutions, the activity can be seen as being equal to the concentration [95, pg. 19].

A common setup for potentiometric sensors is the ion-selective electrode (ISE). Such devices use a membrane that allows a charge build-up for a specific ion. If such a membrane is separating the solution of interest for the measurement from a reference solution where the concentration of the

analyte is fixed, the potential difference across the membrane will be proportional to the natural logarithm of the ratio of ion activities in each solution [96, pg. 122].

One example of a potentiometric biosensor is the one reported by Shishkanova *et al.* [97], whereas a PVC membrane in an ISE has a single-stranded oligonucleotide as the active components. The hybridisation of these components causes a redistribution of the ion concentration at the membrane's surface, which in turn induces a measurable potential difference across the membrane, as described above.

Conductometric devices

A conductometric biosensing device measures the change in resistivity between two electrodes placed in a solution of interest. Such devices are typically associated with enzyme-based biosensors, whereas a catalysed reaction leads to a change in the ion strength of the solution in which the reaction occurs [76], [77], [98]. Alternatively, the change in resistivity might be due to the decrease in the conductivity across the electrode's surface, such as in the biosensor reported by Yaquida *et al.* [99]. Here, due to the immunoreaction of the immobilized layer of the methamphetamine antibody with the methamphetamine itself, the conductivity across this layer decreases.

Impedimetric devices

A more general technique frequently used in biosensing devices consists of measuring both the resistance, Z', and the reactance, Z'', of the entire electrochemical system in response to a sinusoidaly oscillating potential, which are, respectively, the real and the imaginary parts of the complex impedance [76]. Here, the system includes the solution in which the measurement is conducted as well as the interfaces between the electrodes and the solution, and the electrodes themselves. The frequency f at which the potential oscillates can be swept across a wide range of values. This method is known as electrochemical impedance spectroscopy (EIS) and gives information on the change in the charge dynamics both in the bulk and at the electrodes in response to an analyte [100], as well as allowing a step-by-step characterisation of the surface modification of the electrode during the fabrication of the biosensor [92].

The results of EIS measurements are typically presented as Argand diagrams (with Z'' plotted against Z' for each frequency). These plots can then be fitted by a theoretical model based on an electric circuit that best represents the system under study [83]. For example, one can model the finite conductance of ions in an electrolyte with a resistance R_s, while the interface between the biosensor's surface and the electrolyte can be modeled either by a capacitor in parallel with a resistance R_{leak}, or by a capacitor in parallel with a series combination of a resistor associated with charge-transfer, R_{ct}, and the so-called Warburg impedance, Z_w. The first model is commonly used in non-faradaic systems, in which there is very little charge transfer across the interface and the current is mainly due to processes similar to that of charging a capacitor. The second model is applied to faradaic systems, in which there is significant charge transfer, due to redox reactions, across the interface (associated with R_{ct}) and the Warburg impedance models the diffusion of the electroactive species towards the sensor's surface. In both of these systems, the capacitor is often subtituted by a constant-phase element (CPE), in order to better describe deviations from purely capacitive behaviour. The impedance associated with a CPE is given by:

$$Z_{CPE} = \frac{1}{Q(j\omega)^{\alpha}} \tag{3}$$

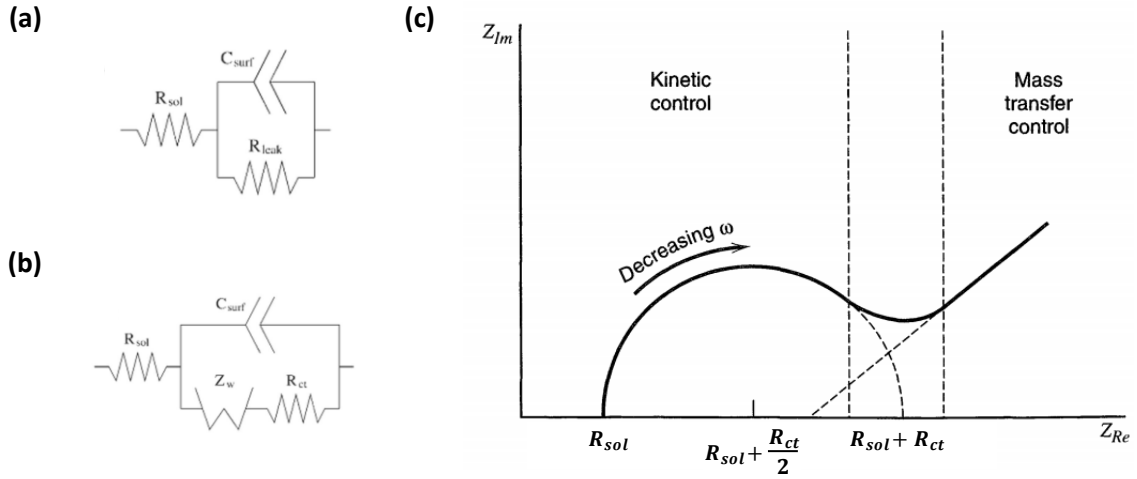

*Figure 7 – The equivalent circuits typically used for **(a)** non-faradaic and **(b)** faradaic processes* [83]. ***(c)** A typical EIS spectrum for faradaic processes* [101, pg. 386].

with Q and α being the two parameters describing the CPE which can be determined by fitting the EIS spectrum. Note that when $\alpha = 1$ the CPE becomes equivalent to an ideal capacitor with capacitance equal to Q. The resulting equivalent circuits for both the non-faradaic and the faradaic regimes are represented in Figure 7.

Models such as these allow to quantify changes in the system under study with the values corresponding to the elements of the equivalent electric circuit. For example, the binding of an analyte to the sensor's surface can be identified as a change in the charge transfer resistance R_{ct} (for faradaic systems), or as a change in the surface capacitance (for non-faradaic systems) [83].

Field-effect transistor devices

Devices based on the field-effect transistor comprise another important class of biosensors [76], [77], [102]. The basic principle of operation of such devices is the same as that of regular FETs: a potential applied at the gate electrode creates an electric field across a dielectric. This field, in turn, alters the conductivity of the conducting channel that connects the source and the drain electrodes, changing the current flowing between said electrodes. In the context of electrochemical sensing, the gate dielectric is typically modified, either by using an ion-selective membrane, in what is known as an ISFET, or by immobilizing on its surface a biocatalitic or a biocomplexing layer, leading to devices such as enzyme (ENFETs) or immunological field-effect transistors (IMFETs or ImmunoFETs).

***

It is worth pointing out that, as with any attempt at a general classification, some devices may not be susceptible to such attempts, as is the case of multimodal biosensors that simultaneously employ several transduction techniques [103]. Another important point is that, when dealing with the subject of different types and operating modes of biosensors, one feels the need for a direct comparison between them, based on the advantages and disadvantages of each one. Such a comparison, besides requiring an extensive review of the published literature, is greatly complicated by the differing experimental conditions and the lack of standardisation in the evaluation of a biosensor's performance. Nonetheless, several useful figures of merit have been defined for this end, which can be extracted from the calibration curve of the sensor. Table 1

Table 1 – Useful figures of merit for biosensor characterisation.

Linear range	The range of concentrations for which the response of the sensor is linear.	-
Sensitivity	The slope of the linear portion of the calibration curve. [104]	$s = \Delta S / \Delta C$
Limit of Detection (LOD)	The minimum amount of analyte that originates a signal that is significantly different from that of a blank sample (containing no analyte). Typically defined as the average signal of the blank sample, S_{bl}, plus three times the standard deviation, σ, of said signal. Note that the concentration corresponding to LOD must then be obtained using the calibration curve. [105, pg. 58]	$LOD = S_{bl} + k\sigma$, with $k = 3$
Limit of Quantitation (LOQ)	Similar to LOD, but with a higher confidence level (typically, 10 times the standard deviation over the blank signal). [105, pg. 58]	$LOQ = S_{bl} + k\sigma$, with $k = 10$
Dynamic range	The ratio of the largest measurable concentration of the analyte and the Limit of Detection. [83]	C_{max} / LOD

presents the most commonly used ones, along with a brief description of their meaning and the formal definitions used in this work.

1.2.2. Nanostructures and the emergence of graphene as a biosensing platform

One of the main focus points of biosensor research is miniaturisation [106]. Motivated by the rise of large-scale and low-cost microelectronics production [76], miniaturisation provides several advantages in terms of improved biosensing performance. In particular, the use of microelectrodes leads to higher sensitivity and faster response, thanks to the hemispherical mass transport profile [106]. Other advantages of miniaturized biosensors stem from the possibility of development of implantable devices for local sensing, multisensory arrays and portable systems for easy diagnostics and monitoring, which are of great interest to the so-called lab-on-a-chip and micro total analysis systems. In these devices, a complete on-site medical check-up can be performed using a single device with no need for a complete laboratory setup. More importantly, biosensors of smaller size allow working with lower volumes of samples and expensive biological reagents and materials. Coordination with techniques such as lithographic patterning [107]–[109] and microfluidics [110]–[112] is an important step towards successful miniaturisation of biosensors.

Nanomaterials and nanostructures are a particularly important part of the miniaturisation of biosensing devices. The reduced size of such structures means that a higher portion of their atoms is located at the surface, where it is exposed to the surrounding environment, as opposed to the interior. In other words, nanostructures possess a high surface-to-volume ratio. This results in a higher sensitivity towards external influences, such as those of an analyte that comes in contact with the nanostructure, which in turn improves the signal-to-noise ratio of biosensors based on such structures [76], [113]. Gold nanoparticles are extensively used, both in optical biosensors, where localised surface plasmon resonance is exploited, and in electrochemical biosensors, where the nanoparticles are used as “electron wires” in place of mediators or as an immobilisation platform [114]–[116]. Quantum dots, especially those based on Cd chalcogenides, are also an important element in many biosensors, thanks to their optical and electronic properties that allow their use as fluorescent labels and make possible the exploitation of fluorescence quenching [117],

[118]. Sensors based on nanowires [119] and magnetic nanoparticles [88], [120] are some of the other applications of nanostructures in biosensing.

A particularly promising class of nanostructures for biosensing applications is that of carbon-based nanomaterials, thanks to their chemical stability, biocompatibility, and excellent mechanical properties [121], [122]. Nanocrystalline diamond, for example, has been used as an immobilisation platform both in biocatalytic [123] and in bioaffinity sensors [124]. Fullerenes have also been used to modify the electrodes in electrochemical biosensors, in order to reduce the potential required for the oxidation reaction of adenine and guanine [125], as well as mediators in enzymatic glucose biosensors, thanks to their advantageous electrochemical properties [126]. However, the most widely applied carbon nanomaterials are carbon nanotubes (CNTs) and graphene [104], [127].

Carbon nanotubes have attracted a lot of attention due to the combination of chemical stability and mechanical strength with excellent electrical conductivity, which lead to their application as a pathway for direct electron transfer between enzymes and the electrode in biocatalytic sensors [128], [129]. Furthermore, CNTs are highly sensitive to the adsorption of molecules on their surface [130], a property that has been exploited in biosensing [131]. Photoluminescence of certain types of single-wall carbon nanotubes (SWCNT) is another property useful for sensing applications [132]. The thin-film arrangement of CNTs in a laterally-oriented network known as buckypaper has also been used as a substrate in biosensors [133].

Graphene, on the other hand, not only matches and even surpasses CNTs in terms of electrical, mechanical and chemical properties (see Section 1.1.1), but also addresses two main issues faced by CNTs in the context of biosensing performance [134]. The first one lies in the morphological structure of CNTs which leads to difficulties in their spatial control and assembly. Graphene overcomes this by being highly susceptible to microfabrication through traditional techniques such as lithography and e-beam patterning, among others. The second issue faced by CNTs relates to the presence of metallic impurities inherited from the synthesis processes, which hinder their performance in electrochemical sensors [135]. Moreover, graphene based materials show lower levels of $1/f$ noise than CNTs [136], [137] and a wider potential window in which it does not react with the electrolyte [138].

An important step in graphene's application in biosensing is its functionalisation [139]. Graphene's electrochemical electron transfer can be greatly increased by the creation of specific functional groups at its surface [140]. Furthermore, functionalisation of graphene can improve its processing by solvent-assisted techniques and facilitates the attachment of the target-specific recognition elements in bioaffinity sensors [21].

One way to overcome the need for functionalisation while still taking advantage of some of graphene's unique properties is to use graphene oxide (GO). This graphene-related material possesses oxygen-containing functional groups, such as carboxyls and hydroxyls, with a carbon to oxygen atoms ratio between 2 and 3 [15]. A reduction (either chemical, electrochemical or thermal) of GO leads to reduced graphene oxide (rGO), with an atomic percentage of oxygen of around 5-10% [92]. The presence of such groups disrupts the sp^2-hybridized network of carbon atoms, leading to a low electrical conductivity in GOs, while some of it is restored in rGOs [141]. Nonetheless, GOs and rGOs are widely used in electrochemical biosensing due to the possibility of attaching the sensing element or the analyte itself to these functional groups [92], [139].

In the case of pristine graphene, there's been a lot of effort directed towards the development of stable, homogeneous, reproducible and simple surface modification techniques. Among these are covalent functionalisation methods, which consist of covalently bonding the functional groups of interest to graphene's surface. For example, free-radicals can be used to directly bond a molecule to graphene's surface. This is exploited in several works with diazonium salts, whereas aryl radicals are formed, with their subsequent attachment to graphene [142], [143]. Alternatively, by hydroxylating the graphene's surface one can attach organosilanes such as 3-Aminopropyl-triethoxysilane (APTES), which then act as linker molecules between graphene and a specific bioreceptor [138]. Other covalent functionalisation strategies are described in several reviews on the matter [139], [144]. One must note that any type of covalent functionalisation disrupts graphene's sp^2-hybridized electronic network, negatively impacting its electronic properties [139]. In fact, covalent functionalisation can be seen as the introduction of defects into graphene's structure.

In order to maintain graphene's excellent electronic properties, several non-covalent functionalisation techniques have been developed. A typical strategy is to take advantage of strong $\pi - \pi$ interactions between graphene and the aromatic rings of linker molecules, such as those of pyrene-, thionine- and porphyrine-based compounds [21]. Another approach consists of functionalisation with polymers, such as polyaniline (PANi), a conducting polymer which can be directly polymerized from an aniline monomer solution on top of graphene [138]. The PANi layer then serves as an attachment point for an antibody, for example. A disadvantage of noncovalent functionalisation relative to the covalent one is a lower stability over time and chemical conditions [145]. An extensive review of non-covalent functionalisation techniques has been published by Georgakilas *et al.* [146].

Perhaps one of the most prominent uses of graphene in biosensing is in FET devices [15]. Here, this material excels thanks to its high carrier density and mobility, as well as its low intrinsic noise. More importantly, graphene's electronic properties (and, consequently, its conductivity) can be modulated by minute external influences such as those of an analyte. In particular, graphene's Fermi level is sensitive to external electric fields, which can be induced by a charged molecule [147]. A shift in the Fermi level results in a change of the carrier density, and, thanks to graphene's zero band gap, can result in a change in the type of the charge carriers (from holes to electrons and vice-versa). Other sensing mechanisms rely on direct charge-transfer between an analyte and graphene, the introduction (or attenuation) of carrier scattering and the change of the local dielectric environment [21].

The variation of graphene's conductivity can be monitored by plotting the current across the graphene channel (I_{DS}) vs the gate voltage (V_G), with the latter being applied either by an electrode under the conducting channel, in a configuration called backgated FET, or by an electrode immersed in an electrolyte which, in turn, comes in contact with graphene. The latter configuration is known as liquid gate and operates thanks to the electrical double-layer formed at the graphene/electrolyte interface, which acts as the gate dielectric [148]. The I_{DS} vs V_G plots, also designated by transfer curves, are V-shaped for single-layer graphene, reflecting its ambipolarity. The minimum of such a transfer curve is the voltage for which the Fermi level lies at the Dirac point. When a charged analyte, such as an antigen, approaches graphene's surface, the electric field caused by the analyte gets imposed on the field created by the gate electrode, shifting the Fermi level and, accordingly, the minimum of the transfer curve. By monitoring this shift (either by tracing the entire transfer curve for each analyte concentration or by fixing a gate potential and by measuring the

corresponding I_{DS}), the analyte's concentration can be quantified (Figure 8). Alternatively, if the analyte induces a change in the mobility of graphene's charge carriers, the slope of the transfer curve will change in accordance. Here, by fixing the gate potential at an appropriate value and by monitoring the change in I_{DS} for that potential, one can relate this change to the analyte's concentration (Figure 8).

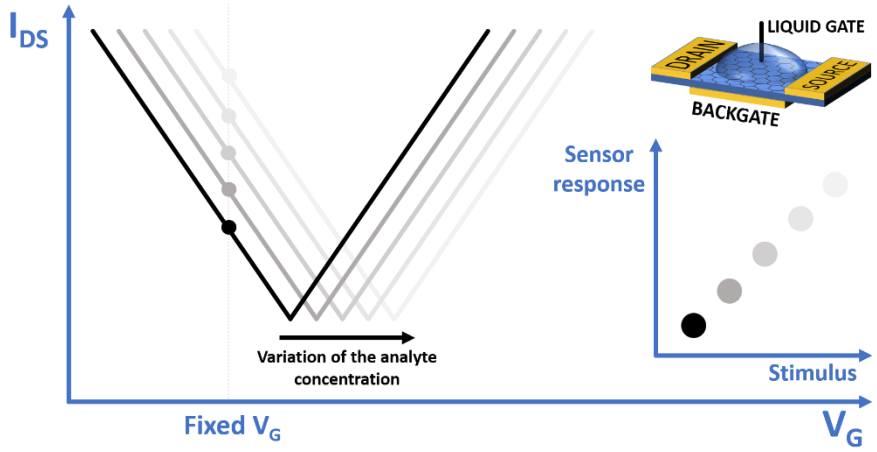

Figure 8 – The measurement mechanism of a GFET sensor. The analyte solution is placed on top of the graphene conducting channel, leading to the shift of graphene's Fermi level and, consequently, its transfer curve. The sensor response in this case is the drain-source current (I_{DS}) change at a fixed gate potential (V_G), with the latter being be applied wither by a back or a liquid gate.

Several examples of GFET-based biosensors have been reported in literature. Y. Ohno *et al.* [148] demonstrated the potential of GFETs as a biosensing platform by measuring the concentration of BSA attached onto graphene's surface in a Phosphate Buffer Saline solution, which acted as the electrolyte of the liquid gate. G. Xu *et al.* [149] developed an array of GFET biosensors functionalised with biotinylated single-stranded DNA (immobilized on CVD graphene with biotinylated BSA and streptavidin molecules) capable of sensing $100\ fM$ of target DNA. Bacteria detection with GFET biosensors has also been shown by Y. Huang *et al.* [150]. Here, CVD grown graphene was non-covalently modified with 1-pyrenebutanoic acid succinimidyl ester, in order to immobilize anti-*E. coli* antibodies. By monitoring the change in the conductivity of the graphene channel at a fixed gate voltage in response to different concentrations of *E. coli* bacteria, a LOD of $10\ cfu/ml$ was achieved. More recently, L. Zhou *et al*. [151] reported a CVD-grown GFET biosensor for carcinoembryonic antigen, using the same linker (1-pyrenebutanoic acid succinimidyl ester) for the antibody. The GFET was operated at $-0.3\ V$ gate voltage, on account of a more significant change in the transfer curves for different concentrations of the analyte at this potential. A LOD of $100\ pg/ml$ was achieved for real-time measurements.

Also of note is the application of graphene in impedimetric biosensors. As covered in the previous section, the binding of an analyte to the sensing surface can be identified by the changes in the EIS spectra of the biosensor. S. Eissa *et al.* [143], for example, developed an impedimetric biosensor by covalently functionalising CVD graphene with 4-carboxyphenyl diazonium salt, for further immobilisation of the anti-ovalbumin monoclonal antibody. By fitting the faradaic EIS spectra corresponding to different concentrations of ovalbumin, a relationship between the percent change of the charge transfer resistance of the chosen equivalent circuit and the logarithm of ovalbumin concentration was established. The reported LOD was of $0.9\ pg/ml$. A. H. Loo *et al.* [152], on the other hand, achieved detection of the rabbit IgG protein using CVD-grown graphene

as a platform for the physical adsorption of the anti-rabbit IgG antibody. A resistance value, which the authors attributed to the charge transfer process, was extracted from the EIS spectra and the relative changes of this parameter were used as the concentration dependant signal. The selectivity of the sensors was verified by exposure to proteins other than the rabbit IgG. The reported linear range was $0.1 - 100\ \mu g/ml$, with an estimated LOD of $0.134\ \mu g/ml$.

***

In summary, a careful look at the status of biosensor research reveals the importance of graphene as a transducer in such devices. This is justified not just by the excellent properties that make this material highly attractive for the development of sensitive biosensing platforms, but also by the prospect of fast, low-cost and simple to use biosensors for on-site diagnostics. This class of biosensors is highly desirable in order to overcome the need for complex analysis techniques, such as the Enzyme-Linked Immunosorbent Assay (ELISA) or mass spectrometry, which, despite their high sensitivity and low limits of detection, require expensive equipment and highly trained personnel for their execution [138].

With this in mind, the objective of this work is to develop a biosensing device with graphene as a transducing element, by (1) synthesising, transferring onto a suitable substrate and characterising graphene, by (2) studying and optimising its functionalisation through different strategies and by (3) demonstrating its operation as a biosensing platform. To address the first part of this objective, graphene samples will be grown by Chemical Vapour Deposition and transferred onto Si/SiO_2 substrates for further characterisation. The second part of the main objective will be tackled by exploring both a covalent and a non-covalent functionalisation strategies. More specifically, the target-specific probes (biotin and anti-hCG) will be attached to the amine groups of either the 3-Aminopropyl-triethoxysilane (APTES), covalently immobilized on graphene hydroxylated by the Fenton reaction, or the pyrene butyric hydrazide (PBH), non-covalently immobilized by the $\pi - \pi$ interactions. The third part of the main objective will be addressed by measuring the response of the sensors to different analytes (avidin and hCG), through the use of the appropriate target-specific probe.

2. Experimental

2.1. Graphene synthesis and transfer

Graphene was grown on 25 μm-thick copper foil ($> 99.99\%$, *MTI*), in a Thermal Chemical Vapour Deposition (TCVD) reactor (Figure 9).

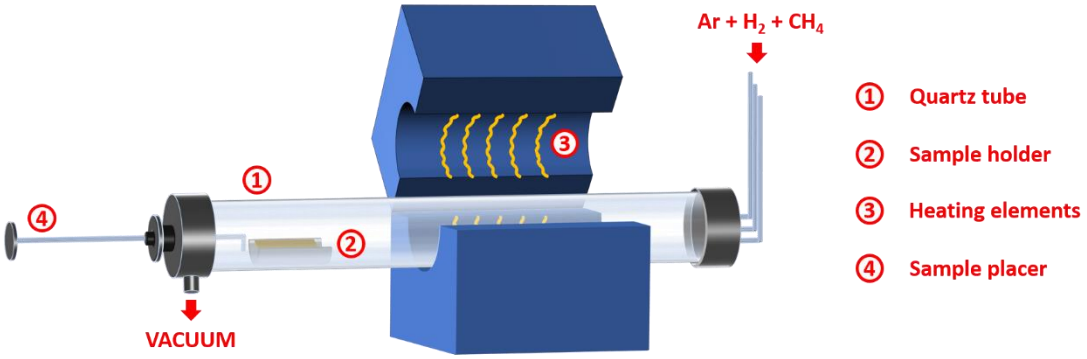

Figure 9 – TCVD reactor used in this work and its main components.

To remove any impurities from the copper substrates and to etch away the native oxide from their surface [153], the substrates were subjected to the following procedure: ultrasonic bath in acetone (15 min), ultrasonic bath in isopropyl alcohol (IPA, 15 min), rinse in isopropyl alcohol, dip into acetic acid (1 min) and rinse in distilled water. The substrates were then dried under a stream of air.

The reactor was preheated to 950˚C and the substrate placed at the edge of the quartz tube, in a sample holder also made of quartz. The synthesis process can be divided in different phases. Figure 10 summarizes the conditions in each one of them.

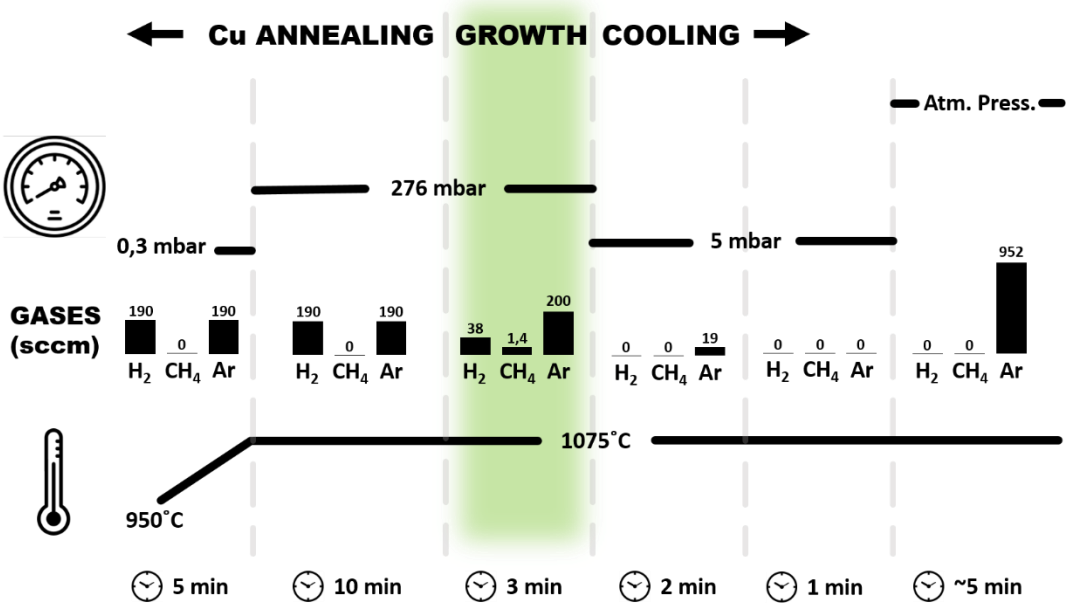

Figure 10 – Stages of the synthesis process of graphene. The sample is placed at the centre of the quartz tube at the start of the annealing stage, which begins with a temperature ramp, and pulled out at the end of the growth stage, highlighted in green, thus initiating its cooling. The temperature of the furnace, however, remains the same until the tube is purged with Ar and the pressure inside reaches atmospheric pressure.

As soon as the pressure reached $0.3\ mbar$ and the gas fluxes stabilised, the sample was moved to the centre of the reactor. The purpose of the annealing phase is two-fold: increase the grain size of copper and clean the impurities from its surface [154]. During the growth phase, methane was introduced into the reactor, providing the carbon atoms for the synthesis of graphene. Hydrogen plays the role of an additional catalyst, assisting in the dehydrogenation of the surface-adsorbed methane. Consequently, the radicals resultant from the methane decomposition migrate towards the graphene nucleation sites (either substrate defects or carbon dimers also formed by the catalytic decomposition of the precursor), adding to the already existing graphene domains. Given that the precursor decomposition is a surface-catalysed reaction, the growth of graphene should be self-limiting, that is, once the entire substrate is covered no further methane decomposition should occur. At the end of this phase the sample was pulled to the edge of the reactor. The reaction chamber was purged with argon so that methane is removed from the reactor, cutting the supply of carbon atoms. After that, the reactor was shut off and the sample was left to cool to room temperature.

Before the functionalisation process could be optimized, the as-grown graphene had to be transferred onto insulating substrates so that its surface modification could be monitored electrochemically. For this, Si substrates with $300\ nm$ layer of SiO_2 were chosen, thanks to the contrast enhancement such substrates provide for the visualisation of graphene sheets [65].

The target substrates for the transfer process were subjected to the following cleaning procedure: ultrasonic bath in acetone (15 min), ultrasonic bath in isopropyl alcohol (15 min) and rinse in isopropyl alcohol.

The transfer was accomplished by the electrochemical bubbling technique [155]. The advantage of this technique relative to others commonly used, such as copper film etching, for example, is its simplicity, faster processing time and reduced cost. Firstly, the copper foil along with the graphene grown on it was cut into $\sim 1\ cm^2$ samples. To prevent the formation of cracks and tears in graphene during the transfer process, a thin layer of PMMA (poly(methyl methacrylate)), average MW 550 000, *Alfa Aesar*), $4.5\%\ w/w$ in anisole, was spincoated onto the sample, according to the following recipe: spread the PMMA solution with a Pasteur pipette so that it covers the entire sample, 1600 rpm (45 s with a 3 s ramp), 3500 rpm (15 s with a 3 s ramp). Next, the samples were loaded into a furnace at 180˚C, for 20 min, in order to cure the PMMA polymer layer. The step after that consisted of dipping the sample into an aqueous solution of NaCl while applying a negative potential to it ($-8.0\ V$). The circuit is closed with a graphite electrode. The electrolysis of the solution leads to the formation of gas bubbles at the exposed parts of the copper foil. These bubbles are the ones separating the graphene+PMMA film from the copper foil, leaving it floating at the top of the solution. It was then scooped out with a microscope slide and placed into distilled water, followed by a bath in deionized water, in order to wash away the salt and any other impurities. Next, the sample was scooped out with the target substrate (Si/SiO_2) and a gentle jet of compressed air was used to remove the water and any air bubbles in between the graphene and the substrate, as well as to straighten out any folds or wrinkles. Afterwards, the sample was placed in a furnace at 180˚C, for 20 min, in order to soften the PMMA film and allow the graphene to accommodate to the surface of the substrate [156]. Lastly, the samples were left in acetone overnight, to dissolve the supporting polymer film. The entire procedure is summarized in Figure 11.

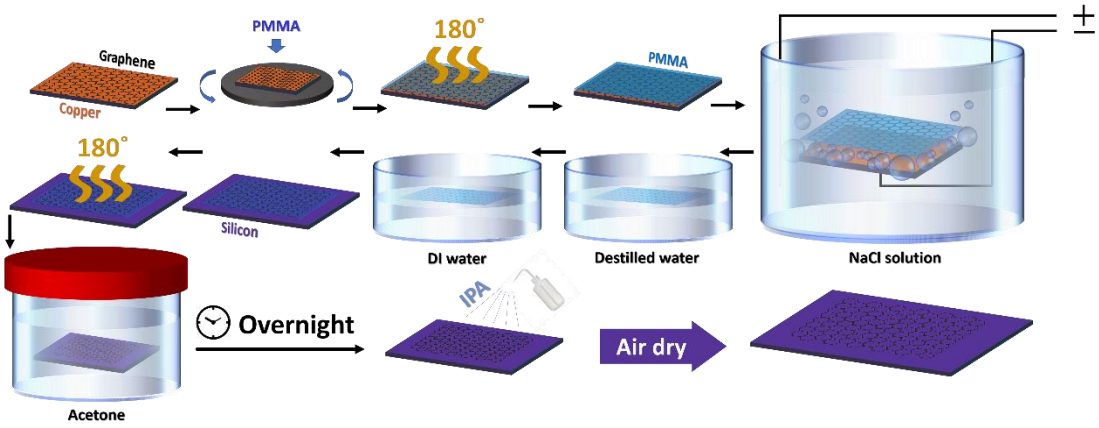

Figure 11 – Transfer process of graphene, from the copper foil on which it is grown onto the Si/SiO_2 substrate.

2.2. Functionalisation

The objective of functionalisation is to immobilize the antibody or the target-binding protein on graphene's surface. In the case of biotin, a vitamin with excellent affinity towards avidin [157], as well as for anti-hCG, the antibody of the human chorionic gonadotropin hormone, this can be done by attaching, to graphene, compounds with amine groups that can then bond to the carboxyl (COOH) groups of biotin or the anti-hCG antibody [20]. To do so, two approaches have been tested in the present work (Figure 12).

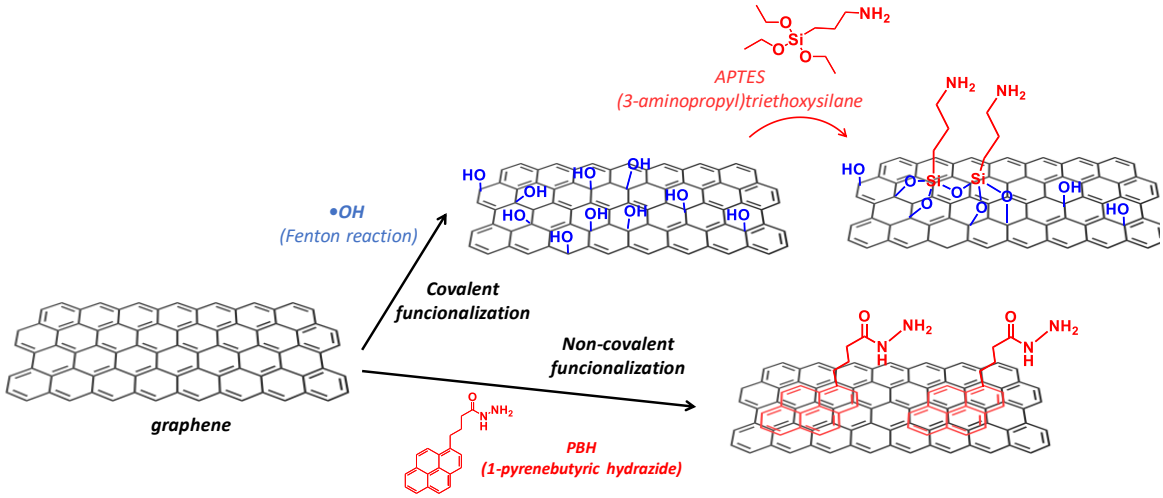

Figure 12 – Functionalisation approaches explored in the present work. The NH2 groups are then used to anchor the target-specific recognition elements (biotin or anti-hCG).

The first approach consists of using 3-Aminopropyl-triethoxysilane (APTES), a compound that possesses the amine group required to bind to the bioreceptor. APTES can be immobilized onto surfaces terminated with hydroxyl groups [138]. Thus, it is necessary to hydroxylate graphene. The Fenton reaction has been used to hydroxylate carbon nanotubes [158]. This reaction is typically described by the following chemical equation:

$$Fe^{2+} + H_2O_2 \rightarrow Fe^{3+} + OH^- + {}^{\bullet}OH \qquad (4)$$

It is the ${}^{\bullet}OH$ that is believed to hydroxylate graphene structures, through the attack at π orbitals in sp^2-hybridized carbon. It is worth noting, however, that there's still debate over the formation of ${}^{\bullet}OH$ during the Fenton reaction [159].

The general procedure of the hydroxylation of graphene by the Fenton reaction can be described as follows: $FeSO_4$ was dissolved in an aqueous solution of H_2SO_4 and then H_2O_2 was slowly added afterwards. This reaction is highly exothermic and is accompanied by violent bubbling that can damage the graphene film. Thus, a wait time of 15 minutes was introduced in order to let the reaction calm down before the introduction of the sample into the mixture.

As will be discussed in Section 3.2.1, the hydroxylation attempts undertaken in the present work were unsuccessful and as such, the APTES immobilization stage was not reached.

The second immobilisation approach consists of non-covalently attaching to graphene a compound with amine groups. Pyrene-based compounds have been used in non-covalent functionalisation of graphene, through $\pi - \pi$ interactions between the two (see Section 1.2.2). Pyrenebutyric hydrazide (PBH, *Sigma-Aldrich,* $\geq 97.0\%$ purity) has been used here, as it possesses the desired amine groups where the biotin vitamin or the anti-hCG antibody can attach.

Generally, the PBH was dissolved in a mixture of N,N-dimethylformamide (DMF, $\geq 99.8\%$ purity, *Alfa Aesar*) and DI water (75:25 %v/v). A $50\ \mu l$ drop of this solution was placed on the sample and left there overnight. After this step, the samples were washed first in DMF and then in water, followed by drying in a stream of nitrogen. For the immobilisation of the biotin vitamin, through attachment to the amine groups introduced to the graphene's surface, a solution consisting of $25\ \mu l$ of $5\ mM$ of D-biotin (*Fisher Scientific*), $12.5\ \mu l$ of $0.1\ M$ of N-(3-dimethylaminopropyl)-N'-ethylcarbodiimide hydrochlorine (EDC, *Sigma-Aldrich*) and $12.5\ \mu l$ of $0.2\ M$ of N-hydroxysuccinimide (NHS, *Sigma-Aldrich*, 98%) in Phosphate Buffer Saline (PBS, $pH = 7.4\ 10\ mM$, $200\ ml$/tablet from *Fisher Bioreagent*) solution was prepared. EDC and NHS have the role of activating biotin's carboxylic groups. Similar to the PBH step, a $50\ \mu l$ drop of this solution was placed on the sample and left there for 2 hours. In the case of the anti-hCG antibody, the same procedure was followed, but using $25\ \mu l$ of $1\ mg/ml$ of anti-hCG (mouse monoclonal anti alpha hCG, *Ig Innovation*) instead of D-biotin. The samples were then washed in PBS and dried under a stream of nitrogen.

The optimisation study consisted of testing different concentrations of the PBH solutions, which should result in different surface densities of the PBH molecules on graphene. This, in turn, should have an effect on the number of immobilised target-specific probes (biotin or anti-hCG), affecting the performance of the sensors. Ideally, the surface density of such probes should be as high as possible as long as the analyte can easily bind to the respective biorecognition element. Control samples were also used, incubated in blank solutions (with no PBH), while another one was incubated in PBS (no biotin) after being previously functionalised with PBH.

Lastly, detection tests were conducted by incubating the functionalised samples in different concentrations of the analyte and by measuring the sensor's response, through EIS, after each incubation. In the case of avidin, the incubation consisted of placing $50\ \mu l$ drops of avidin (from eggs, *Panreac Aplichem*) in PBS solution on the samples and leaving it there for 45 min.

In the case of hCG tests, the sensors were passivated after the antibody immobilization, in order to reduce non-specific interactions with graphene that is not covered by PBH molecules. The passivation consisted of placing $50\ \mu l$ drops of a $10\ \mu g/ml$ solution of BSA (Standard Grade Powder from *Fisher Bioreagents*) in PBS on the samples, for 30 min. Afterwards, the samples were washed in PBS and dried under a stream of nitrogen. The procedure for the hCG (full length protein, 95% purity, *Abcam*) sensing tests was the same as that for the avidin tests. Here, a control sample was

also prepared, through the same procedure, using the anti-*E. coli* antibody (*E. coli* serotype O/K Polyclonal Antibody, *ThermoFisher Scientific*) instead of anti-hCG.

2.3. Characterisation

The structural and morphological characterisation of the as-grown graphene was done by Raman spectroscopy, optical microscopy and Scanning Electron Microscopy (SEM). The monitoring of the hydroxylation by the Fenton reaction was done by measuring the contact angle of water before and after the reaction, as well as by Raman spectroscopy. To assess the success of the functionalisation at different stages of the process, X-ray Photoelectron Spectroscopy (XPS) was used. Further optimisation of the functionalisation parameters was monitored by Electrochemical Impedance Spectroscopy (EIS). Differential Pulse Voltammetry (DPV) and Energy Dispersive X-ray Spectroscopy (EDS) were also employed throughout this work.

A brief description of the techniques used, focusing on the technical aspects specific to the analysed samples, is presented below. The relevance, in the context of this work, of the techniques used is also briefly explored. Lastly, technical information regarding the equipment and the measurement-relevant parameters employed here are presented.

2.3.1. Electrochemical Impedance Spectroscopy and Differential Pulse Voltammetry

EIS and DPV measurements were conducted in an electrolyte composed by the $K_4[Fe(CN)_6]/K_3[Fe(CN)_6]$ redox pair ($1\ mM/1\ mM$) dissolved in PBS solution, with the voltage being measured against a Ag/AgCl reference electrode (CHI111, *CH Instruments, Inc*). A VersaSTAT 3 potentiometer (*Princeton Applied Research*) was used. A platinum counter electrode was employed. In order to clearly define the active area of the sample, an o-ring was attached to the bottom of a perforated cup. The o-ring was then pressed against the sample, allowing the cup to be filled with the electrolyte while the sample seals the orifice at the bottom (Figure 13). The electrical contact to the graphene was established using silver paint and silver-plated copper wire. An alternative setup was used for the initial electrochemical characterization of the as-grown samples, where a Teflon ring was glued to the sample's surface using the chemically inert Lacomit Varnish (*Agar Scientific*). The same varnish was used to completely cover (and thus insulate) the sample around the Teflon ring, leaving only its inner area exposed (the electrical contact to the graphene is done prior to applying the varnish, using the same strategy as in the main setup). Note that, despite having the advantage of avoiding the potential damage from the repeated contact

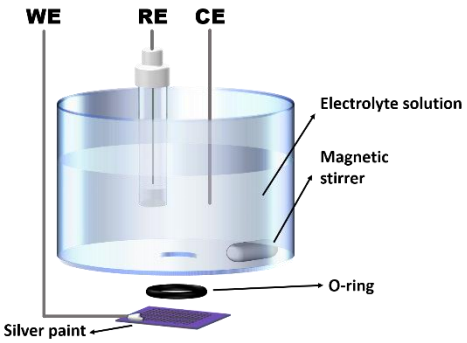

Figure 13 – The setup used for the electrochemical measurements. WE, RE and CE refer to the working, the reference and the counter electrodes, respectively.

with the graphene occurring in the o-ring based setup, this varnish-based one can't be used before the PBH immobilisation step, due to the fact that DMF dissolves the varnish.

The advantage offered by DPV consists in the reduction of the contribution form background currents such as those due to interfacial capacitance [101, pg. 291]. This increases the sensitivity towards faradaic processes. In the present work the base potential was swept between $-0.2\ V$ and $+0.8\ V$ and back.

The EIS measurements were performed at the open circuit potential. The AC signal imposed on top of this potential had an amplitude of $5\ mV$. The electrolyte solution was stirred with a magnetic stirrer, at a constant rate of $500\ rpm$, in order to achieve a diffusion layer of a steady thickness for a given frequency [101, pg. 34-35].

After the measurements, the samples were washed either in DI water (before the functionalisation) or in PBS (during and after the functionalisation), followed by drying under a stream of nitrogen.

The spectra were analysed by fitting the data, using Powell's algorithm, to an equivalent electrical circuit, chosen based on the gathered information about the sample.

2.3.2. Raman Spectroscopy

In the present work, the Raman characterisation was done using a Jobin Yvon HR800 Raman system, by *Horiba*. A He-Cd laser with a wavelength of $441.6\ nm$ (IK series by *Kimmon*) was employed, focused on the sample with a lens with magnification of $\times 100$ and a numerical aperture of 0.8. The resulting Raman signal was collected by the same lens, filtering out the reflected laser light and light due to Rayleigh scattering with an edge filter. The dispersion of the collected light was achieved using a $600\ grooves/mm$ grating, which allowed fast acquisition of spectra in the spectral regions of interest. This was particularly important for Raman mapping studies, where a mobile *xy* stage moves the sample under the incident laser beam, allowing automatic acquisition of Raman spectra inside e predefined area of the sample.

The processing of the data presented in this work consisted of, when necessary, removing a baseline due to the background signal from each of the spectra, as well as by applying a Savitzky–Golay smoothing (fitting 2nd degree polynomials to sections of 9 points each). Raman maps were constructed using the integrated area in the region of the peaks of interest.

The specific parameters of the measurements and data processing varied depending on the sample, the information of interest, and the context of the characterisation.

2.3.3. Scanning Electron Microscopy and Energy Dispersive X-ray Spectroscopy

Scanning Electron Microscopy (SEM) consists of scanning the sample's surface with an electron beam and mapping the intensity of the resultant signal, which is mainly composed by secondary electrons.

For graphene samples, SEM can be used to study their morphology and topology (nucleation centres, wrinkles, etc.) [66]. Perhaps more importantly, SEM can be used to distinguish regions of the sample with a different number of layers [160]. This is possible due to the variation of secondary electron yield with the number of graphene layers, as well as thanks to the attenuation of the secondary electron emission from the substrate [66]. From a practical stand point, due to graphene being just one atom thick, low acceleration voltages must be used, in order to reduce the penetration depth of the electron beam.

In this work, SEM was used to monitor the continuity of the graphene film, its morphology in terms of number of layers, and for identification of any structural defects. The signal was acquired using a backscattered electrons detector, integrated in a Vega 3 SBH system by *TESCAN*.

EDS measurements were also performed in the present work. The employed system, incorporated into the Vega 3 SBH SEM, is based on a Bruker Xflash 410 M Silicon Drift Detector, with a $133\ eV$ energy resolution (at $MnK\alpha$) @ 100 kcps. The detector has an effective area of $10\ mm^2$ and is cooled by a Peltier element. The elements in the range B (5) to Am (95) can be identified and quantified. The software module uses a standardless PB-ZAF method for quantification.

2.3.4. X-ray photoelectron spectroscopy

X-ray photoelectron spectroscopy (XPS) relies on the analysis of the energy of the photoelectrons emitted in response to the incidence of x-rays on the sample.

Here, XPS was used to verify the immobilisation of the different functionalising components (namely, PBH and biotin) on the graphene samples.

The spectra were acquired in an Ultra High Vacuum system, with a base pressure of $2\times10^{-10}\ mbar$. The system is equipped with a hemispherical electron energy analyser (*SPECS Phoibos 150*), a delay-line detector and a monochromatic $AlK\alpha$ ($1486.74\ eV$) X-ray source. High resolution spectra were recorded at normal emission take-off angle and with a pass-energy of $20\ eV$, which provides an overall instrumental peak broadening of $0.5\ eV$.

2.3.5. Surface contact angle measurements

By measuring the contact angle between a droplet of liquid and the sample's surface, changes in surface free-energy of the sample can be monitored.

Contact angle measurements have been used in other works to monitor the surface modification of graphene [20]. In particular, the functionalisation of graphene with pyrene-based compounds has been shown to increase its wettability, resulting in the reduction of the contact angle of water by $\sim10°$.

Here such measurements were performed in an attempt to verify the immobilisation of PBH on graphene, as well as to assess the hydroxylation by the Fenton reaction. Photos of the droplet profile were taken with a regular smartphone camera, with the contact angle being calculated using the *drop_analysis* plug-in for the *ImageJ* software.

3. Results and Discussion

3.1. Graphene synthesis, transfer and characterisation

A Raman map of a $20\times20\ \mu m^2$ area of the as-grown graphene, based on the ratio of intensities of the 2D and G bands, as well as the spectra from three different locations of the map, are presented in Figure 14 (a). Here, the maximum Raman signal value in the range corresponding to the different bands was used as a measure of their intensity. Ideally one should perform a fitting on each one of the spectra that compose the map in order to get the correct intensity. However, this becomes impractical as the number of such spectra increases. Moreover, small local shifts in the spectral position of the G band were observed on the as-grown samples, most likely due to local mechanical stresses [71] arising from inhomogeneities in the copper substrate during its surface restructuring at high temperatures, as well as shifts in the spectral position of the 2D band, due to local variations in the number of layers [71], as discussed below. This impedes one from fixing the peak's spectral position for calculation of intensities. Using the area under the desired peak is also flawed, as the 2D band in multiple randomly oriented layers of graphene is known to widen [71].

The Raman spectrum taken at the spot marked by a blue circle in Figure 14 (a) has a relatively high intensity ratio of the 2D and G bands ($I_{2D}/I_G \approx 1.7$) and is often associated with single-layer graphene. The spectrum corresponding to the point marked by the green circle, which is more representative of the rest of the sample, possesses a lower I_{2D}/I_G ratio (≈ 0.7). The lack of splitting of the 2D band, along with its large value of full-width at half maximum ($FWHM \approx 58\ cm^{-1}$) is

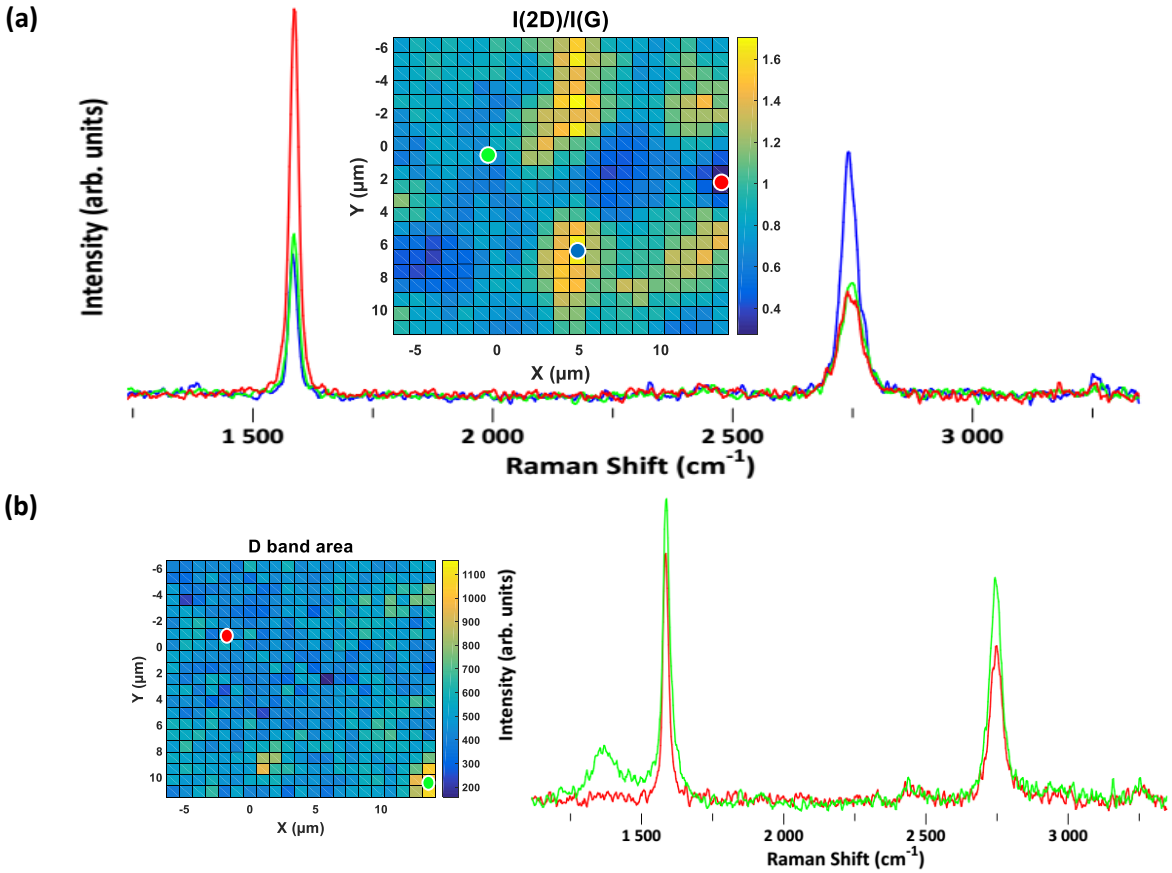

*Figure 14 – **(a)** Raman map of the ratio of intensities of the 2D and G bands of an as-grown graphene sample, along with the spectra corresponding to the three points marked on the map. **(b)** Raman map of the D band integrated area, along with the spectra of the two points marked on the map.*

characteristic of bi- or few-layer graphene with a random relative orientation of the two layers [71]. Finally, the spectrum taken at the point marked by the red circle on the Raman map has the lowest I_{2D}/I_G ratio (≈ 0.3), with a very intense G band (the spectra in Figure 14 (a) were not normalized in order to highlight the increase in the intensity of this band). Similar spectra were observed for bilayer graphene samples with a relative orientation of 12˚ [161].

Figure 14 (b) shows the distribution of the integrated area of the D band, typically associated with defects in graphene (see Section 1.1.3). The spectrum taken at the spot marked by the red dot is representative of most of the sample and shows a negligible D band. This band only appears sporadically, as shown by the spectrum corresponding to the green dot.

The SEM images of the samples give further insight into the samples' morphology. As can be seen in Figure 15 (a), the sample is covered in patches with a darker contrast than the respective surroundings. It is also possible to identify even darker regions inside these patches, such as the ones highlighted in Figure 15 (b). Also of note is their somewhat polyhedral nature, which occasionally presents a hexagonal tendency. Lastly, one should address the ripples seen in the SEM images. These are attributed to copper surface reconstruction [162].

In light of these results, and given the fact that the Raman mapping revealed a complete coverage of the copper substrate by graphene, the dark patches seen in the SEM images can be attributed to few-layer graphene (FLG) islands on top of a monolayer, fully coalesced film. The coalescence of the graphene film was also confirmed by placing the as-grown samples inside a furnace at 180˚C. Given that graphene protects the copper surface from thermal oxidation and is itself immune to it at this temperature, any portion of the copper surface not covered by the graphene film would oxidize, leading to its immediate identification due to the characteristic oxide-induced colour change [163]. No such colour change was observed on the as-grown samples after several hours in the furnace.

The formation of such FLG islands goes against the commonly cited self-limiting growth of graphene on copper, according to which, once the substrate is completely covered by the graphene monolayer, the catalytic effect of copper ceases and no further layers should be formed. As such, it is likely that in these layers are formed simultaneously. This is supported by the lack of splitting

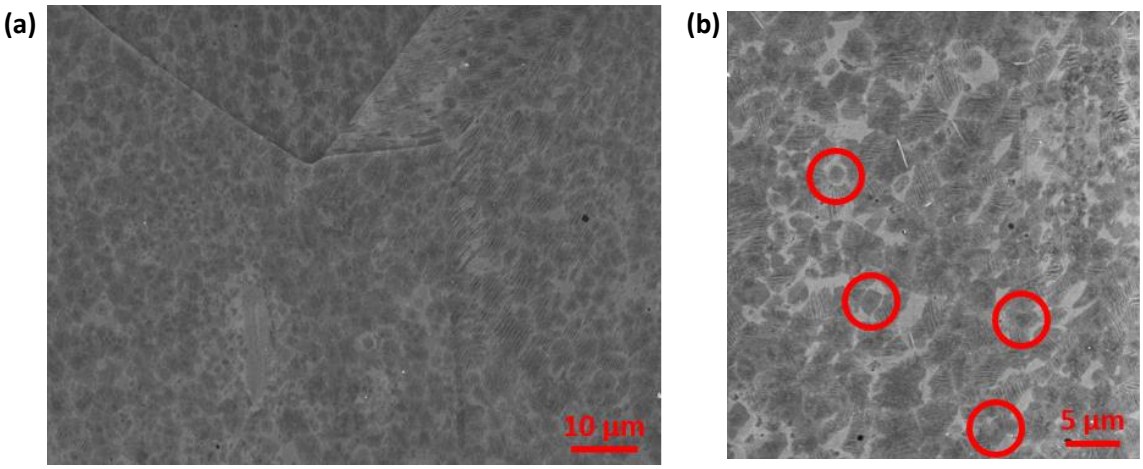

*Figure 15 – **(a)** SEM image of the as-grown graphene sample on the copper substrate. **(b)** Detail of the graphene's morphology. Red circles highlight the presence of smaller, darker patches inside the main ones seen throughout the sample. Both images were taken with an acceleration voltage of 3.5 kV and had their contrast adjusted for ease of visualisation.*

of the 2D band in the Raman spectra of the FLG regions, due to, most likely, the random relative orientation of the layers, since each layer is not constrained by the underlying ones, as those haven't fully formed yet. The catalytic effect of the copper surface is "felt" more by the layers closest to it, which leads to the complete coalescence of the bottom layer, whereas the layers further from the copper grow at a slower rate.

This growth mechanism implies the existence of a nucleation centre common to the various layers. Graphene nucleation sites on copper substrates are typically associated with defects, surface steps and impurities [164], with the latter particularly relevant for the formation of secondary layers [165]. B. Luo *et al*. reported the occurrence of pin holes and amorphous carbon at the nucleation sites of graphene domains [163]. These formations could serve as carbon sources, either directly (in the case of amorphous carbon sites) or as pathways for the graphitic/amorphous carbon ingrained in the Cu bulk (in the case of pinholes) [164]. It is also worth noting that these nucleation centres might be too small to be identified by either SEM or Raman spectroscopy.

Lastly, in light of these conclusions regarding the morphology of graphene, the very low intensity of the D band in the Raman mappings should be addressed. With the presence of FLG islands one would expect a somewhat intense D band, due to the edges of the secondary layers (see Section 1.1.3 regarding the Raman characterisation of graphene). However, the laser spot size used here is large ($\sim 1 - 2\ \mu m$ in diameter), of the order of the size of the FLG islands. Thus, the contribution of the edges to the total signal acquired in a given spot will be very small. Note also that the rather large spot size makes the correct reproduction in the Raman maps of the shape of the FLG islands nearly impossible, which explains why these maps do not appear to directly correlate to the optical microscopy images taken in the same area of the sample.

The transfer of graphene onto silicon revealed to be quite challenging, with a large number of samples rendered unusable after PMMA removal with acetone, due to extensive tearing of the graphene film. Figure 16 shows the same region of the sample before and during the acetone removal step, showing the start of the tearing.

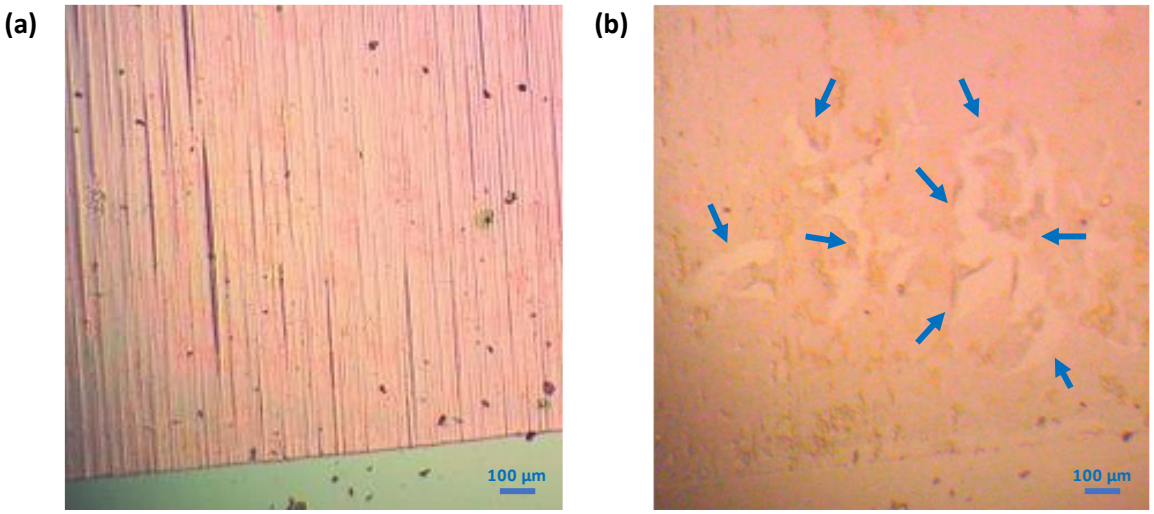

Figure 16 – Optical microscopy images of a graphene sample transferred onto Si/SiO2, ***(a)*** *before and* ***(b)*** *during the PMMA removal in acetone. The arrows point to the tears in graphene. Note how the copper rolling striations are reproduced by the PMMA coating in (a).*

In order to get some insight into the PMMA removal process, a sample (graphene+PMMA on silicon) was placed inside a Petri dish under an optical microscope. Shortly after acetone was added to the dish, the formation of a network of cracks was observed. After some time, one could see the PMMA layer spreading apart along these cracks, in many places pulling the graphene film along (Figure 17).

Initial efforts at solving this issue were directed towards a different way of PMMA removal. Several alternatives to acetone dissolution were explored, such as anisole and ethyl acetate. No significant improvement was observed with these solvents. Attention was then turned to the properties of the polymer itself. Without an immediate reason to doubt the quality of the PMMA solution (as it was prepared in-house and had been used in successful transfers shortly before the start of this work), different baking conditions were tried, both after the spincoating step and before the acetone dissolution (see Figure 11). For all of these the cracking and eventual tearing of graphene persisted.

Lastly, a new PMMA solution was prepared, as described in Section 2.1 ($4.5\%\ w/w$ in anisole). After the separation of the graphene+PMMA film from the copper substrate it became clear, due to the difficulty in the handling of the film as well as the colour it acquired as a result of constructive interference of light, typical of thin films, that the polymer film was thinner than the ones used in the failed transfers, at around $300\ nm$ for the new solution. No cracks were seen forming when the dissolution of these new polymer films was observed under an optical microscope. This resulted in the successful transfer of graphene.

Figures 18 (a)-(c) show the same region of the graphene sample transferred onto a Si+SiO_2 substrate as seen using optical microscopy, SEM and Raman mapping of the I_{2D}/I_G ratio. The islands of secondary layers identified earlier on top of copper are clearly visible in the optical and electronic microscopy images. It is also interesting to note that due to the different distributions of these islands, the grain structure of copper is reproduced by the graphene, even after the transfer. The varying distribution of FLG islands indicates preferential nucleation on specific copper grains, in accordance with the literature, where different crystallographic orientation of the copper grains affects such important processes as precursor decomposition and surface diffusion [165]. The variation in the FLG islands' distribution is made more evident by the high density of secondary layer nucleations along what corresponds to the position of the copper grain boundaries, indicating more favourable nucleation conditions along these lines. Also of note is the visible alignment of the FLG islands along a specific direction, common to all the copper grain regions but more visible only for some of them (due to a lower FLG island density). This is the direction of the copper striations due to the rolling of the films. Such striations have been associated with an increased impurity carbon content, resulting in a higher nucleation density along these lines [164]. This corroborates the hypothesis of ingrained amorphous carbon acting as a carbon source for the simultaneous nucleation of several graphene layers. Lastly, the bright spots seen in the optical microscopy

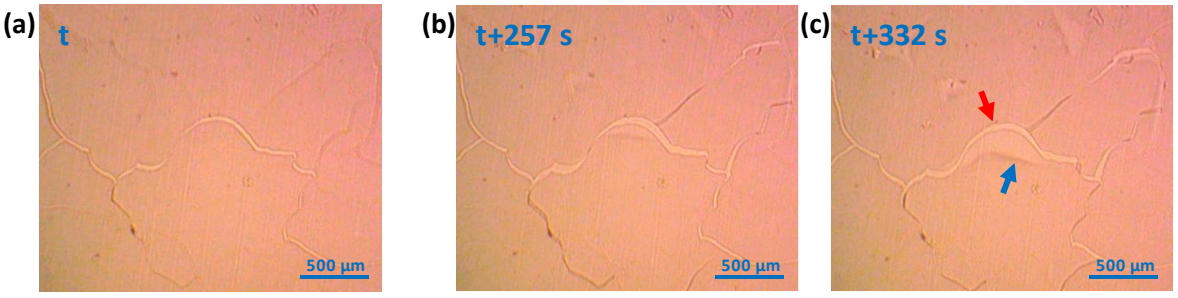

*Figure 17 – The progression of the cracking of the PMMA coating along with the resulting tearing of the graphene film. The rolling up of the teared graphene edge can be seen in **(b)** and **(c)**.*

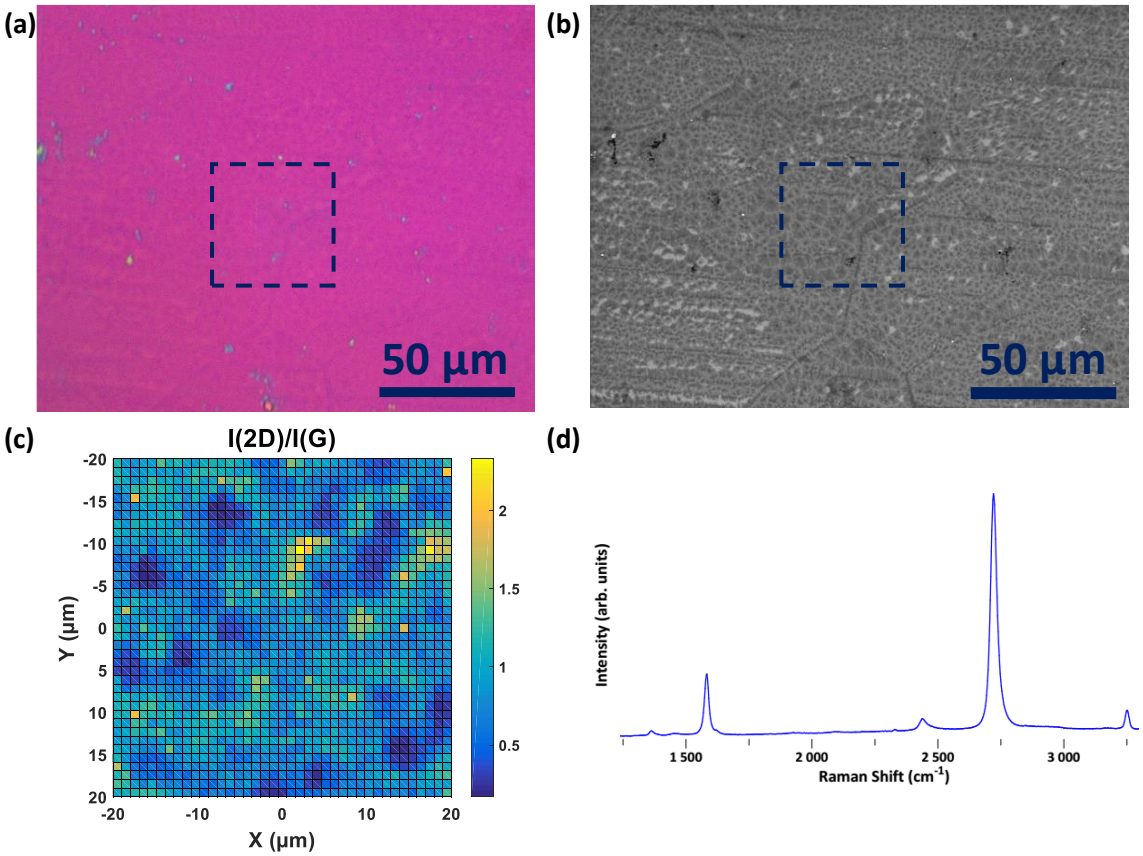

*Figure 18 – The same region of the transferred sample as seen using **(a)** optical and **(b)** scanning electron microscopy (5 kV acceleration voltage). **(c)** A Raman map of the I(2D)/I(G) ratio corresponding to the area delimited in (a) and (b) by the red square. **(d)** A Raman spectrum of a region (not pictured here) between adjacent FLG islands.*

images, the ones that appear as darker regions when seen in SEM, should be addressed. These may be due to PMMA residues left on the sample, as these do not appear on the samples before the transfer procedure (when the PMMA is spincoated onto the sample and later dissolved in acetone). In fact, the presence of PMMA residues after graphene transfer is a well-documented phenomenon [166]. Worth noting is the fact that these residues do not present the characteristic Raman spectrum corresponding to PMMA (data not shown), nor do they appear to be non-conducting, as no charge effect due to electron accumulation is seen in the SEM images (the residues have a dark contrast). This points to the possibility of the residues being an organic product of the interaction between PMMA and acetone.

Also pictured is a Raman spectrum taken at a region between the FLG islands (Figure 18 (d)). This spectrum is characteristic of single-layer graphene and corroborates the previously given description of the sample as being a single, fully coalesced graphene layer with FLG islands on top.

To complete the characterisation of the samples, electrochemical measurements were done. Figure 19 (a) presents an EIS measurement of one of the as-grown samples. The observed impedance is very large, without any clear indication of charge transfer across the electrode (no semicircle). This raises the possibility of the lack of electrochemical activity for the redox pair used ($K_4[Fe(CN)_6]/K_3[Fe(CN)_6]$). However, using Differential Pulse Voltammetry (DPV), one can see two distinct peaks which disappear when the measurements are made in PBS (no redox pair). This confirms the occurrence of redox reactions involving the $K_4[Fe(CN)_6]/K_3[Fe(CN)_6]$ pair. The origin of

this electrochemical activity can most likely be attributed to the few-layer islands' edges, as the electron transfer is known to dominate at graphene's edges, relative to the basal plane [167].

As such, the EIS measurements are performed in the faradaic regime. As discussed in Section 1.2.1, the interface between the electrode (sample) and the electrolyte in this regime can be modelled by a CPE[2], C_{surf}, in parallel with a charge transfer resistance, R_{ct}, both connected in series with the resistance of the electrolyte, R_s (identified as R_{sol} in Figure 7). The Warburg resistance appears in series with R_{ct}. Note that in this context, R_s represents not just the solution resistance, but also all the contact resistances in series with it.

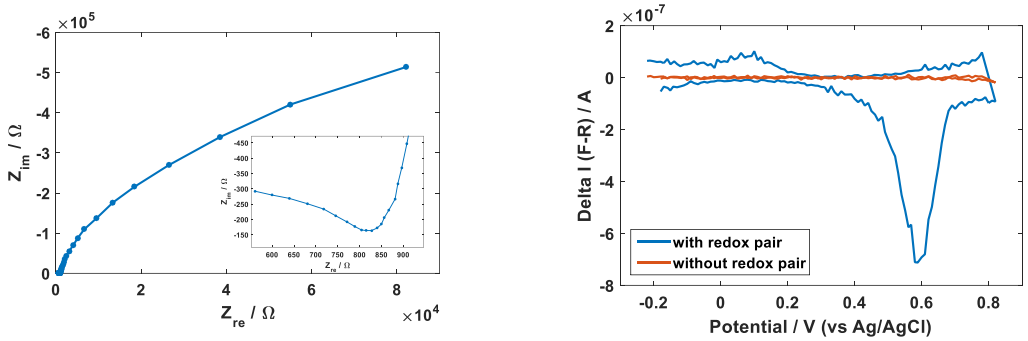

*Figure 19 – **(a)** An EIS spectrum of the as-grown graphene (100 kHz to 1 Hz). The inset gives a more detailed look at the high frequency region. **(b)** DPV curves resultant from the measurements performed in PBS with and without the presence of the $K_4[Fe(CN)_6]/K_3[Fe(CN)_6]$ redox pair.*

The EIS spectra collected in this work are more complex than the ones associated with this simple equivalent circuit, presenting a small semicircle in the high-frequency range (inset of Figure 19 (a)), possibly due to the phase shift caused by the reference electrode [168]. This semicircle is not fully defined (for frequencies above $100\ kHz$ the spectrum becomes too noisy), which makes an accurate fitting of this region impossible. At the same time, reaching the low-frequency range, where diffusion and convection begin to play an important role, is impractical as the time required for the acquisition of each data point increases as the frequency decreases. Thus, the $100\ Hz - 1\ Hz$ region was chosen to be fitted and the Warburg component was dropped from the equivalent circuit described above (due to the fact that R_{ct} dominates completely over Z_W in this frequency range).

For a correct interpretation of the results it is important to relate the changes in the parameters describing the components of the equivalent circuit to the changes in the surface properties of the samples. Here, the charge transfer resistance, R_{ct}, is expected to change as a result of the interaction with the analyte. As the different compounds are successively immobilized on graphene's surface, any charge transfer across the sample's surface should be affected, either by blocking the access to the electrode's surface or by electrostatic interactions with the immobilised compounds, for example (Figure 20). The parameters of C_{surf} itself may also change, due to the differences in the charge distribution on graphene's surface as the different compounds are immobilized. As for R_s, the resistance of the solution itself (or any other resistance in series with it) should not alter significantly.

[2] The use of a CPE instead of a pure capacitor is justified by the inhomogeneity of the sample's surface, due to the FLG islands.

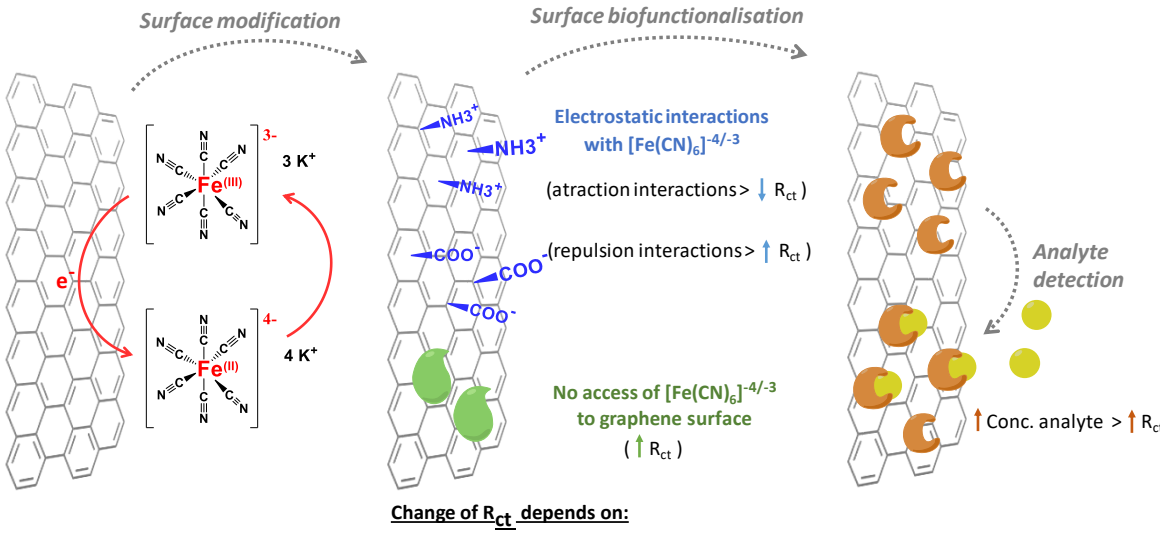

Figure 20 – Influence of the functionalisation process and the interactions with the analyte on the R_{ct} parameter.

One last consideration regarding EIS concerns an issue that became apparent after repeated measurements on the same sample. The repeated contact between the sample and the o-ring of the measurement setup often lead to partial degradation of the graphene film at the contact point. This results in two possible consequences: (1) the electrical contact to the active area of the sample is worsened, increasing the resistance R_s and (2) if in subsequent measurements the damaged region is placed in contact with the electrolyte, the active area of the graphene sample will be diminished. The second consequence was minimized by aligning the contact patch of the o-ring with the ones of the previous measurements, using a small drop of the electrolyte to centre the measurement area with the o-ring delimited opening in the electrolyte container. The downside of this strategy is the possibility of further damage to the graphene. This, however, is not critical as long as some electrical contact to the graphene inside the o-ring delimited area remains and has no effect on the sensing-relevant parameters (those associated with the CPE and with R_{ct}).

3.2. Functionalisation and bioanalyte detection

A table summing up all the samples used in this section, as well as the characterisation and the functionalisation procedure these were subjected to, can be found in Annexes.

3.2.1. Covalent

The covalent functionalisation strategy becomes particularly interesting in light of the graphene morphology described in the previous Section. The existence of the few-layer islands can provide an anchoring point for the bioreceptor molecules without directly affecting the underlying monolayer.

Table 2 summarises the different parameters tested in the present work in an attempt to hydroxylate graphene by the Fenton reaction.

Table 2 – Parameters tested for the Fenton reaction.

Samples	1st round of experiments: 30 min	2nd round of experiments: Overnight
F1	**Reaction A:** • 250 mg $FeSO_4$ • 2.50 ml H_2O_2	**Reaction C:** • 250 mg $FeSO_4$ • 0.25 ml H_2O_2
F2	**Reaction B:** • 250 mg $FeSO_4$ • 1.25 ml H_2O_2	**Reaction D:** • 500 mg $FeSO_4$ • 1.25 ml H_2O_2

Note: Each reaction contains 1 ml of H_2SO_4 (0.1 M). The total volume of reaction was kept at 10 ml (pH=3). A wait time of 15 minutes was introduced in order to let the reaction calm down before the introduction of the sample into the mixture

The results of both rounds of experiments were assessed by Raman maps. An increase in the intensity of the D band is expected, given the fact that the bonding of the OH groups to the graphene alters the hybridisation of the carbon bonds, from sp^2 to sp^3 [20]. As such, the distribution of the ratios of the integrated areas of the D and G bands across $23\times22\ \mu m^2$ maps, taken after each round of experiments, was plotted (Figure 21).

The first round of experiments did not result in a significant increase in Area(D)/Area(G) ratio, leading to the conclusion that little or no hydroxylation has occurred.

The amount of Fe(II), H_2O_2, and the [Fe(II)]:[H_2O_2] ratio are important parameters for the success of the Fenton reaction [169]. As such, two new reactions (C and D) were attempted, with an altered set of parameters. Namely, the reagent concentrations were altered while the reaction time was also significantly lengthened. The immediately apparent result was the formation of a precipitate, which started accumulating non-uniformly on the sample's surface (Figure 22 (a)). The Raman mapping analysis revealed a general increase in the D band intensity, especially in the case of Reaction C, where this increase was more pronounced (see Figure 21).

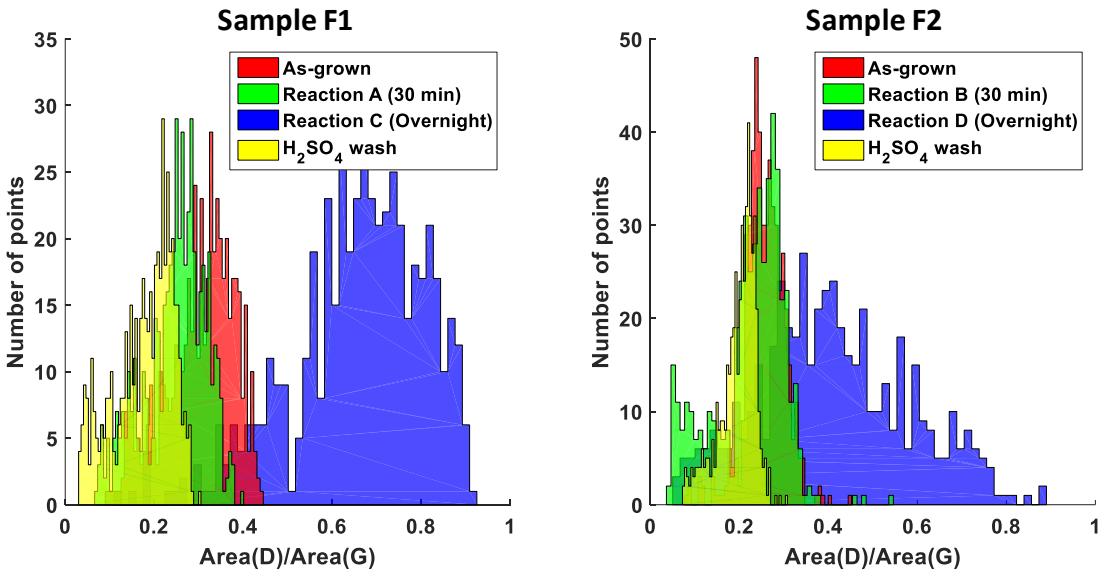

Figure 21 – The distribution of the area ratios of the D and G Raman bands across $23\times22\ \mu m^2$ regions of the samples, for the different reactions and treatments that these samples were subject to.

*Figure 22 – Optical microscopy images of the same graphene sample **(a)** before and **(b)** after Reaction D, as well as **(c)** after the H_2SO_4 wash. The insets show the corresponding contact angle measurements.*

As for the precipitate, EDS measurements were performed in order to assess its nature. A high iron content was detected at the precipitate agglomerates (data not shown here). Given that the presence of such precipitate is undesirable for these samples, a sulfuric acid (H_2SO_4, $0.1\ M$) treatment was performed, first by simple washing and then by immersion for two hours. Optical microscopy showed a nearly complete removal of the precipitate (Figure 22 (c)). The contact angle increased after the acid wash (82˚), but did not reach the value of the as-grown sample, which might be either due to some degree of hydroxylation remaining after the procedure or due to the contribution of some residual precipitate to the surface's roughness. Raman mapping showed the return of the D band intensity back to the initial level (Figure 21), going against the hypothesis of the sample being hydroxylated. As such, the slightly reduced contact angle, relative to the as grown sample, is most likely justified by the presence of residual precipitate.

With the hydroxylation attempts undertaken in the present work being unsuccessful, the APTES immobilization stage was not reached. The covalent functionalization strategy was thus abandoned.

3.2.2. Non-covalent

The first batch of PBH-functionalised samples (with varying concentrations of PBH) was first studied by Raman spectroscopy. As can be seen in Figure 23, where the Raman spectra were normalized with respect to the G band of graphene, besides an increase in the intensity of the D band, accompanied by its apparent splitting, several new peaks appear in the spectra of PBH-functionalised samples. Namely, a double-peak structure can be identified at around $\sim 1250\ cm^{-1}$, as well as a broad peak at $\sim 1510\ cm^{-1}$ (a 0.6 neutral density filter had to be used in order to reduce the laser power incident on the sample, as otherwise the intensity of these peaks appeared to diminish with successive spectrum acquisitions). The spectral position of the peak at $\sim 1622\ cm^{-1}$ is consistent with that of the D' band. Similar peaks have been identified by M.

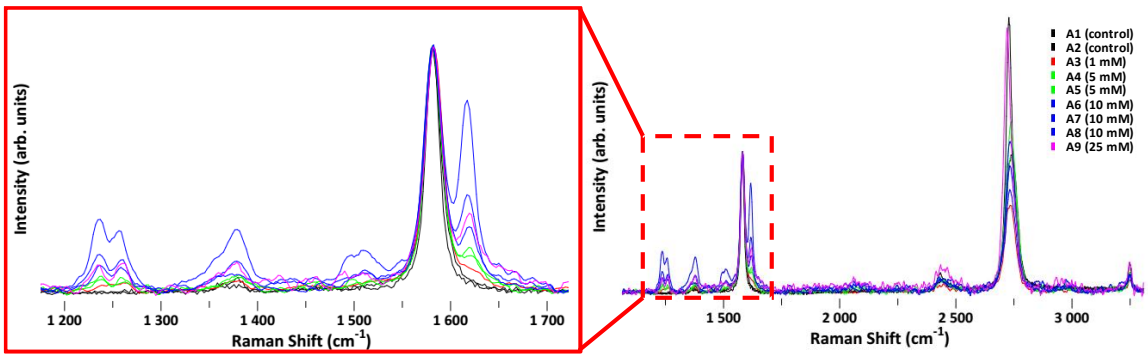

Figure 23 – Raman spectra after PBH functionalisation, revealing the appearance of new peaks. The spectra were acquired with a $442\ nm$ excitation wavelength and normalised to the G peak. The background contribution was subtracted and a smoothing function applied, as described in Section 2.3.

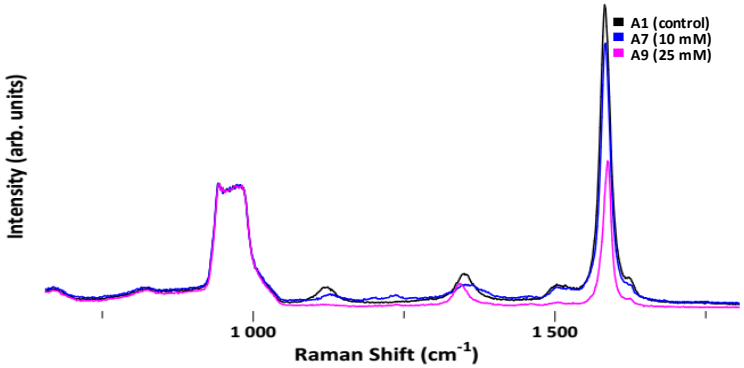

Figure 24 – Raman spectra of PBH-functionalised samples, acquired with a $532\ nm$ excitation wavelength. The spectra were normalised to the intensity of second order Si peak (just below $1000\ cm^{-1}$).

Hinnemo *et al.* [170] on monolayer graphene functionalised with pyrene butyric acid (PBA), a compound similar to PBH, but with a carboxyl group instead of an amine one[3]. Other peaks attributed to PBA in [170] appear at $1140\ cm^{-1}$, $1400\ cm^{-1}$ and $1560\ cm^{-1}$. Here, no peak at $1400\ cm^{-1}$ could be distinguished from the background noise (despite being one of the strongest for pure pyrene [171]), while the peak at $1560\ cm^{-1}$ is too close to the G band of graphene to be clearly identified, even with a proper fitting. As for the one at $1140\ cm^{-1}$, no such peak was identified in the present work. However, when a $532\ nm$ laser was used, a broad peak appeared at $\sim 1114\ cm^{-1}$ (Figure 24), with its intensity diminishing as the concentration of PBH increased. This peak cannot be attributed to PBH as it was present on all samples, including the control ones which were never in contact with PBH. These samples, however, were incubated in the solvent mixture used to dissolve PBH (DMF:H_2O, 75:25 %v/v), which suggests the possibility of the DMF/water mixture leaving some sort of contaminant or residue (such as a precipitate) responsible for the unidentified peak (note that for pure DMF, the closest peak to this spectral position is the one at $1094\ cm^{-1}$, with no peak at $\sim 1114\ cm^{-1}$ [172]). Moreover, the broad band at $\sim 1510\ cm^{-1}$ was also observed on the control samples, using a $532\ nm$ excitation wavelength. Both of these peaks disappear from the control samples when using a $442\ nm$ laser, with only the one at $\sim 1510\ cm^{-1}$ remaining for the PBH functionalised ones. The origin of these peaks remains unknown. Nonetheless, the fact that under $442\ nm$ excitation the peaks at $\sim 1250\ cm^{-1}$ and at $\sim 1510\ cm^{-1}$ only appear on PBH-functionalised samples should be a clear indicator of the immobilisation of this compound on top of graphene, supported by the increase in intensity of the D' peak at $\sim 1622\ cm^{-1}$. Moreover, the functionalisation appeared to be uniform as the results were consistent for over 25 spectra for each sample.

Note that, based on Figure 23, no conclusions regarding the surface density of the immobilized PBH can be taken based on the relative intensity of the PBH-related peaks. Even though the spectra were normalised to G band's intensity, for ease of visualisation, this intensity varies throughout the same sample. Furthermore, the relation between the surface density of PBH and the intensity of the PBH-related peaks, may not be straightforward. Compounds based on aromatic rings may bond to graphene according to different geometries, specially once intermolecular interactions are considered [170]. These variations in bonding geometry may have an effect on the vibrational properties of the mentioned compounds, as well as on the properties of graphene itself, which, in turn, should affect the Raman spectrum of the sample.

[3] Another noteworthy difference is the excitation wavelength used in [170], which was of $532\ nm$.

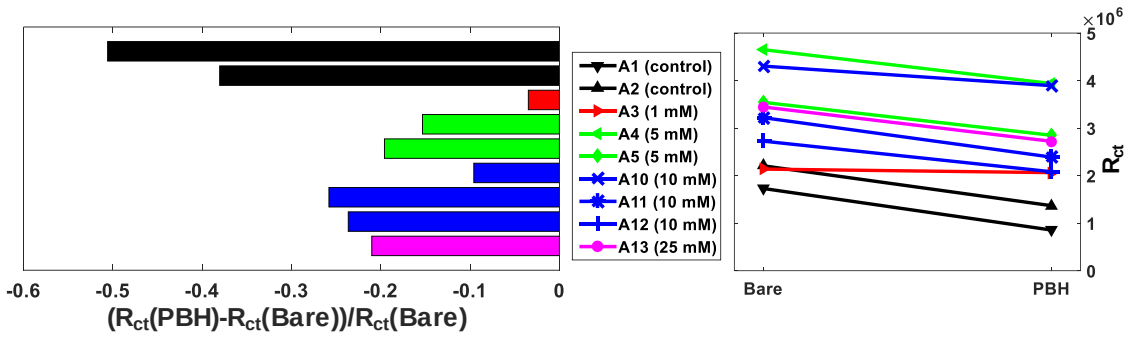

Figure 25 – R_{ct} variation as a result of PBH immobilisation (right-hand side). The left-hand side of the Figure shows the relative variation of this parameter. In the legend, the concentrations refer to the concentration of PBH for each sample. Samples functionalised with the same concentration are presented in the same colour.

Contact angle measurements were performed in an attempt to gain more clues regarding the surface density and orientation of the immobilized PBH molecules. However, no significant change in its value was observed.

Attention was then turned towards EIS analysis. After fitting the acquired data to the equivalent circuit model described previously, a reduction in R_{ct} was observed for all the samples (Figure 25). Firstly, the behaviour of the control samples should be addressed. These samples showed the largest reduction in the charge transfer resistance value, despite only being in contact with the DMF/water mixture (no PBH). Such a reduction might be related to the possibility of DMF-related contaminants or residues being left on the surface of graphene, proposed previously as an explanation for the unidentified Raman peaks observed under $532\ nm$ excitation. The presence of such residues could cause an increase in the charge transfer across the sample surface. Another possible explanation would be the creation of DMF induced defects in the graphene films, as DMF is one of the most commonly used solvents for dispersion of graphene sheet, and, in the preliminary tests conducted in this work (not shown here) was seen to induce tearing of the graphene film. Partial tearing of graphene during incubation in the DMF/water mixture could expose new graphene edges, increasing the charge transfer. This possibility, however, is countered by the lack of any significant increase in the intensity of the D band in the Raman spectra of the control samples, which should have increased had the partial tearing been responsible for the decrease of R_{ct}.

As for the PBH functionalised samples, the mechanism behind the reduction of the charge transfer resistance is not entirely clear, with the unexpected behaviour of the control samples discussed above complicating the interpretation of the results. The markedly different response of the Sample A10 from the other two incubated in the same concentration of PBH is also puzzling. However, as mentioned previously, the few-layer islands' edges are most likely responsible for the electrochemical activity of the as-grown sample. Assuming that the immobilised PBH molecules are oriented parallel to graphene's surface (and, thus, bond to the basal plane of graphene), the reduction of R_{ct} may be justified by the occurrence of charge transfer across PBH, resulting in electrochemical activity at the basal plane. As such, no immediate conclusion regarding the optimal PBH concentration can be reached.

As for the other equivalent circuit parameters, the ones associated with the constant phase-element, C_{surf}, showed little variation throughout the entire functionalisation process and are not

discussed here, while the observed variations of R_S (not shown here) can be explained based on the graphene film damage by the contact with the o-ring.

Moving onto biotin immobilisation, XPS measurements were performed in order to verify this protein's presence on the samples after this step of the functionalisation process. Figure 26 (a) shows the overall XPS spectra of a sample with PBH ($10\ mM$) and of a sample with both PBH and biotin (these spectra were calibrated to the binding energy of the silicon 2p electrons in SiO_2 [173]). Besides the expected peaks due to carbon and those originated mainly by the substrate (silicon and oxygen), nitrogen and chlorine peaks can also be observed in both spectra. While the presence of nitrogen can be justified by the immobilisation of pyrene and biotin (with both of these compounds containing this element)[4], the chlorine-related peaks are most likely due to the adsorption of Cl^- from the PBS solution, since it contains a great amount of NaCl ($0.137\ M$). Moreover, given that the PBH functionalised samples are washed in DMF and water, the fact that these peaks can be observed in both spectra indicates that this adsorption occurs either during the electrochemical measurements (which are made in a PBS electrolyte solution) or after, when the samples are removed from the measurement setup and some electrolyte may evaporate before the samples are washed with DI water.

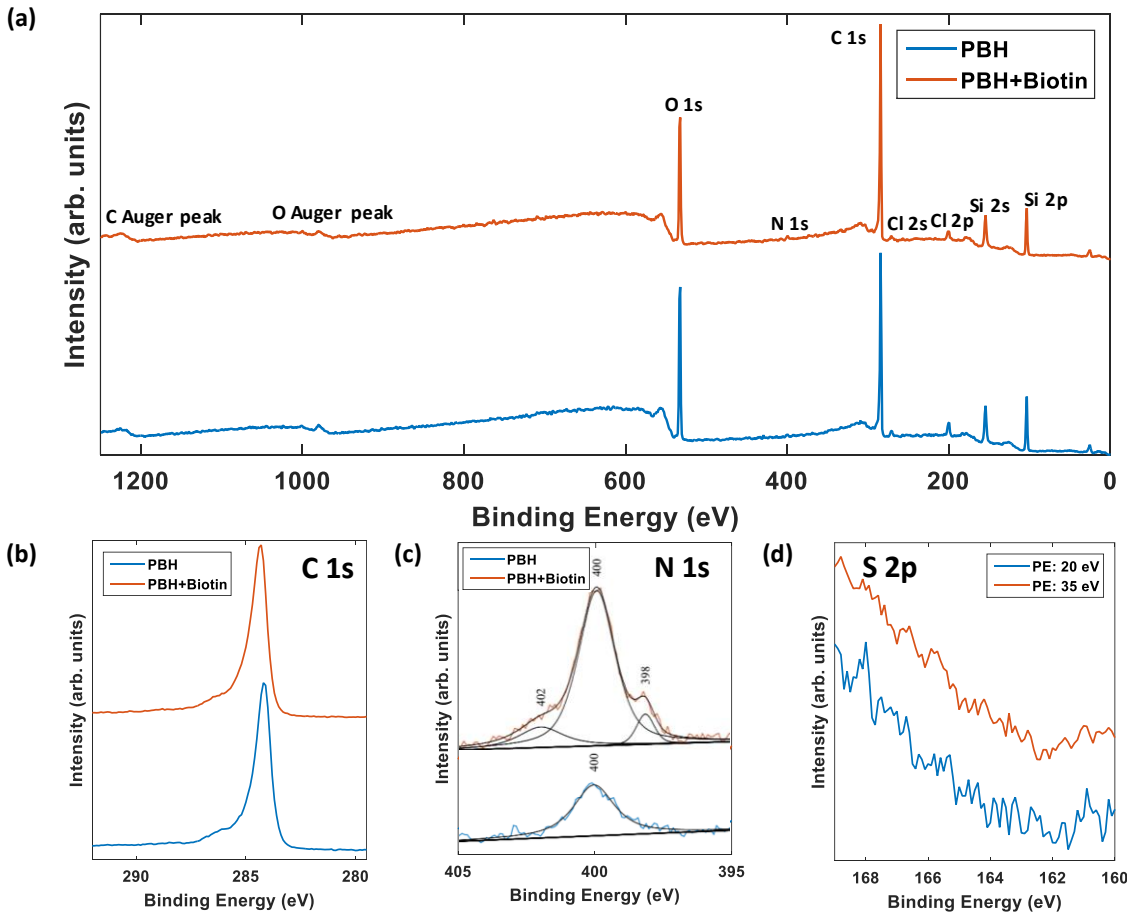

Figure 26 – XPS spectra of PBH- and biotin-functionalised samples. ***(a)*** *Overall spectra, with the identification of the observed peaks.* ***(b)-(c)*** *High-resolution spectra comparing the regions corresponding to the (b) C 1s and (c) N 1s peaks.* ***(d)*** *Spectral region corresponding to the S 2p peak's binding energy of the biotin-functionalised sample, for two different Pass Energy values.*

[4] Note also that DMF, EDC and NHS all contain nitrogen.

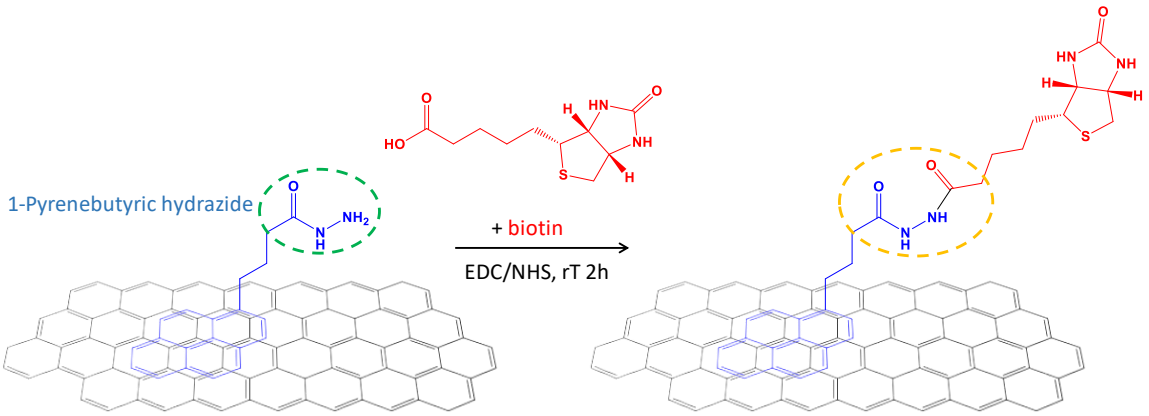

Figure 27 – Biotin's bonding to the PBH molecule. In green, the hydrazide group that contributes to the XPS peak at $\sim 400\ eV$. In yellow, the bond contributing to the two new peaks in the XPS spectra.

A closer look at the C 1s peak (Figure 26 (b)) reveals no significant change neither in its structure nor in its relative intensity as a result of biotin immobilisation. This is in accordance with what should be expected, as the main contribution to this peak comes from graphene itself and no direct binding to it should occur during biotin immobilisation. The presence of a small peak at $\sim 286\ eV$ in both spectra, typically associated with $C - O$ bonds [174], may be attributed to the previously described organic residues due to incomplete PMMA removal after the transfer procedure.

As for the peak due to photoelectron emissions from the N 1s orbitals, the peak at $\sim 400\ eV$ is most likely due to hydrazide groups (-CONH-NH_2) present in PBH [175]. More interestingly, the comparison of the spectra before and after incubation in the biotin solution (Figure 26 (c)) reveals the appearance of two new peaks after this functionalisation step. The one at $\sim 402\ eV$ has been reported as a result of bonding between hydrazide and carboxyl groups [176]. Finally, the peak at $\sim 398\ eV$ can be attributed to the N-N bond [177] (present in PBH), which is altered after biotin's bonding to the amine groups. The bonds of interest for this discussion are highlighted in Figure 27.

Lastly, in order to verify the presence of sulphur in the biotin functionalised sample (as no sulphur is expected to be present on the sample prior to this step), a high-resolution measurement was conducted in the energy range corresponding to the binding energies of the S 2p electrons ($160 - 170\ eV$) (Figure 26 (d)). However, no clearly resolved peak was observed, even after the variation of the electron Pass Energies. This may be attributed to the closeness of the referred peak to the one corresponding to Si 2p photoelectrons, with the background due to inelastic energy loss of these photoelectrons possibly obscuring the sulphur peak [178].

A new round of EIS measurements was performed. Here, sample A10, previously functionalised with $10\ mM$ PBH, was incubated in PBS, without the presence of neither biotin nor EDC/NHS, in order to act as a control. The rest of the samples were functionalised with the same concentration of biotin, as described in Section 2.2. Figure 28 shows the evolution of the R_{ct} value throughout the entire functionalisation process, with the left-hand side of the figure showing the relative variation of this parameter in response to biotin immobilisation.

Generally, apart from sample A10, a large reduction in R_{ct} was observed. This indicates that the presence of biotin has a charge transfer resistance-lowering effect. The exact mechanism by which this occurs is unknown. In the case of samples A1 and A2 (no PBH) the decrease in R_{ct} might point towards adsorption of biotin, without actually bonding to graphene. Moreover, the significant

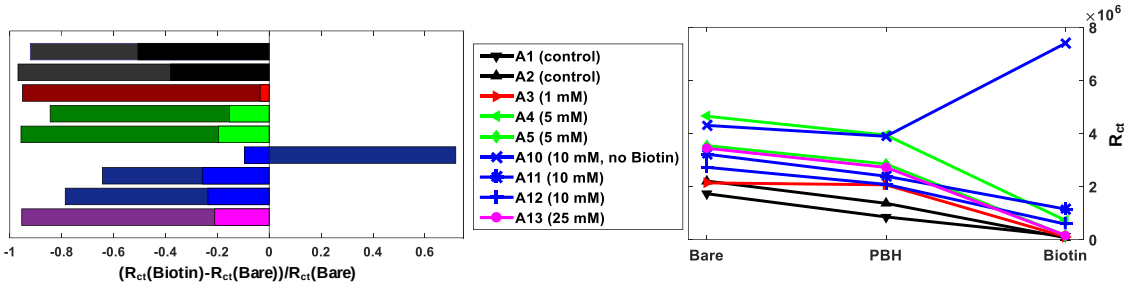

Figure 28 – R_{ct} variation throughout the functionalisation process. The left-hand side of the Figure shows the relative variation of this parameter (the brightly coloured bars correspond to variations after PBH immobilisation, and are displayed here for comparison/tracking). The right-hand side shows the absolute values of R_{ct}. In the legend, the concentrations refer to the concentration of PBH for each sample. Samples functionalised with the same concentration are presented in the same colour.

increase in the R_{ct} value of sample A10 points to the existence of additional, yet to be considered, interactions.

In most simple terms, when the sample is incubated in a solution, three types of changes can be expected: (i) one or several compounds are immobilized on the sample's surface, either chemically or physically, (ii) a component of the surface is removed, or (iii) the surface is modified through rearrangement of the already present components. Note that several such processes may be occurring simultaneously.

On sample A10, given that R_{ct} increased above the base value measured before the entire functionalisation process, any kind of process of type (ii) would imply the removal of something that was present on the as-transferred graphene, before the start of the functionalisation process. Other than some PMMA residues, no other contaminants have been observed on the as-transferred samples. Given that no effect on PMMA is expected after a two-hour incubation in PBS, the occurrence of process (ii) on sample A10 cannot be used to justify the increase in R_{ct}. In what concerns processes of type (i) on the same sample, only PBS-related adsorption can be reasonably considered as possible during the functionalisation step in question (such adsorption has been previously considered as a possible explanation for the presence of chlorine peaks in the XPS spectra of both PBH- and biotin-functionalised samples).

Lastly, any surface modification (process (iii)) would imply either direct damage to the graphene film, or the rearrangement/modification of the previously immobilised PBH. Damage to the graphene film would expose new edges, resulting in an increased residual charge transfer (smaller R_{ct}), while no reports of PBS-induced PBH rearrangement/modification mechanism were found in the literature.

Thus, based on the EIS results for Sample A10, the R_{ct} increase can be tentatively attributed to PBS-related adsorption (either on its own, or through interaction with graphene or PBH). The exact mechanism by which this increase occurs remains unexplained and requires further investigation. Note also that this speculative discussion of the results assumes that all the immobilisation processes performed here are stable at the time scale of the experiments (for example, that no degradation of the immobilised PBH occurs before the next step) and that the application of potential to the sample during the EIS measurements does not cause any alteration to its surface. Both assumptions were confirmed by repeated EIS measurements at the same stages of the functionalisation process, which resulted in stable, reproducible results. The above discussion also doesn't take into account the possibility (which was previously presented as a possible explanation

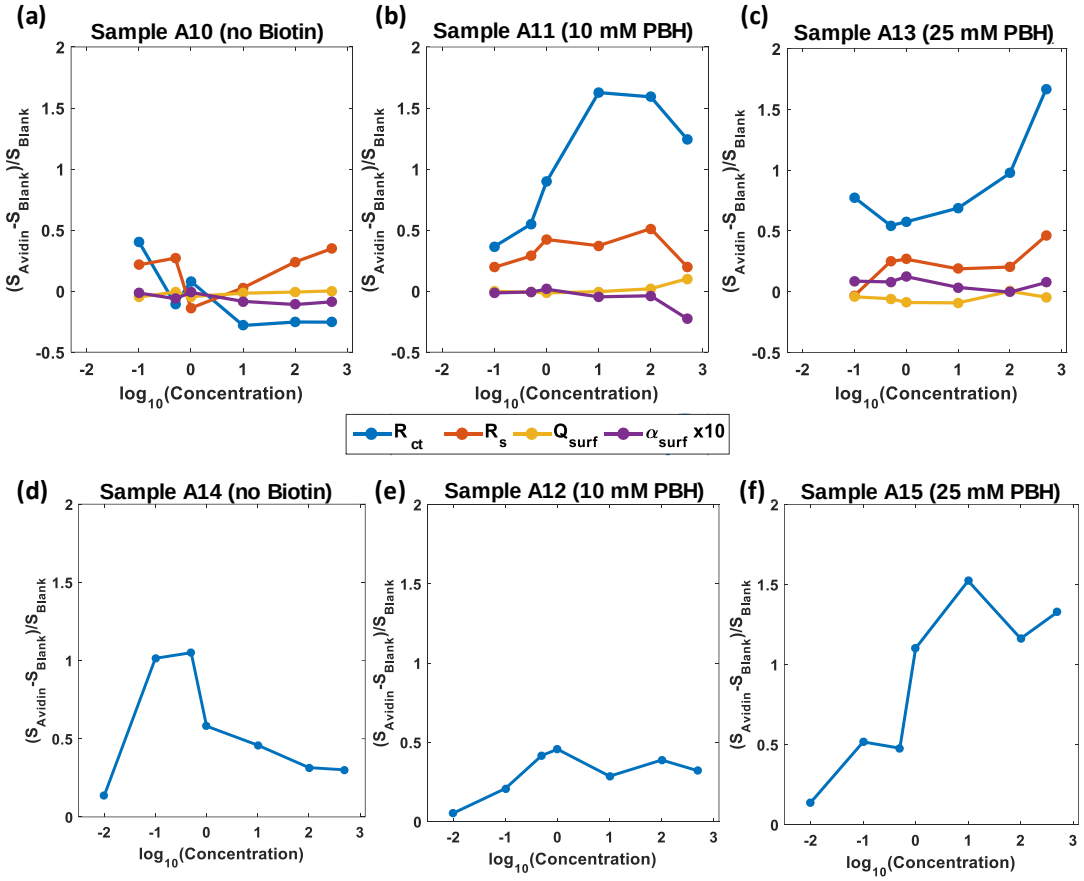

Figure 29 – Relative variations of the equivalent circuit parameters (together designated by S, for "signal") in response to different concentrations of avidin, for six different samples. Samples A10 and A14 were modified with 10 mM of PBH, but no biotin immobilisation took place.

of the Raman results) of DMF-related contamination being present on the samples, as any attempt to consider this occurrence before it is confirmed and the contaminant identified would be pointless.

As this simplistic model is largely unsupported in terms of the information available in the literature (with a significant amount of publication failing to provide an explanation for the charge transfer variation), further investigation is required in order to detailly explain the interactions occurring on the sample's surface during the functionalisation process and EIS measurements. Until then, any conclusions regarding optimal functionalisation parameters based on this model will be strictly in the realm of speculation.

Moving onto the biosensing tests, samples A10, A11 and A13 were chosen for testing the detection of avidin. Figures 29 (a)-(c) show the results, presenting the variation of all the parameters extracted from EIS spectra fittings in response to different concentrations of avidin.

Focusing on the R_{ct} parameter, a larger response for the biotin-functionalised samples is evident. Also, broadly speaking, R_{ct} appears to increase for higher concentration. However, this trend is not clear enough to allow any definitive conclusions regarding the performance of these biofunctionalised electrodes. Furthermore, detection tests performed on replicas of these samples (Figures 29 (d)-(f)) showed a somewhat different behaviour, with only the sample A15, the one functionalised with 25 mM of PBH, showing a response larger than the control sample (A14, the

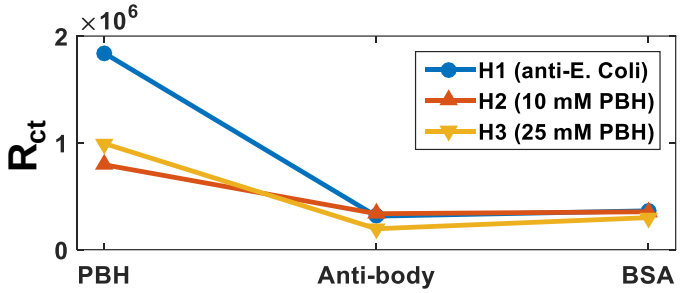

Figure 30 – Variation of the charge transfer resistance, R_{ct}, throughout the functionalisation procedure (for hCG detection tests).

one without biotin). Nonetheless, it is worth mentioning that a non-monotonic variation of the biosensor signal has already been reported in the literature, with no explanation offered as for the reasons behind such behaviour [152].

As for the other parameters obtained from fitting the EIS spectra (not shown in Figures 29 (d)-(f)), once again, no sensor-like behaviour was observed.

In a last attempt to validate the functionalisation procedure employed in this work, hCG detection tests were performed after the immobilisation of the anti-hCG antibody and passivation with BSA. An anti-*E. coli* functionalised sample was used as a control. The varnish-based setup described in Section 2.3.1 was used for these samples.

In all the samples, the immobilisation of the antibody, be it anti-hCG or anti-*E. coli*, resulted in a reduction of the R_{ct} parameter, which then increased slightly after passivation with BSA (Figure 30). Once again, the mechanism by which the antibody immobilisation leads to an increase in charge transfer is unknown. As for the passivation step, an increase in R_{ct} was expected, as the whole idea behind this step was to reduce the non-specific interactions with graphene's surface, which should make the redox pair's access to graphene (and the consequent charge transfer) more difficult. Moreover, the low magnitude of this increase in R_{ct} can be explained taking into account that the BSA passivation should only affect the exposed graphene (areas that are not covered by the PBH molecules) and that the charge transfer at the unmodified graphene is already very low (based on the high impedances observed for the as-grown graphene). This also points to the conclusion that the antibody plays the main role in the charge transfer process, which in turn would

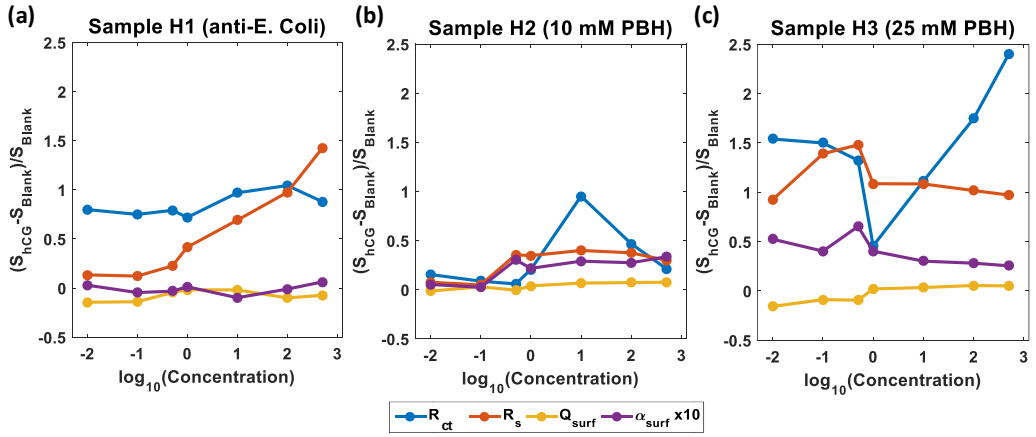

Figure 31 – Relative variations of the equivalent circuit parameters (together designated by S, for "signal") in response to different concentrations of hCG, for three different samples. Sample H1 was modified with $10\ mM$ of PBH and anti-E. coli antibody (instead of anti-hCG).

explain the considerable reduction in R_{ct} after its immobilisation. As such, the attachment of the analyte to the antibody should reduce the contribution of the latter to the charge transfer, increasing R_{ct} as the concentration of the bonded analyte increases.

The biosensing tests for these samples were performed by evaluating the change in the EIS spectra in response to different concentrations of hCG. As seen in Figure 31, the response of samples H2 and H3 is larger than that of the control sample (H1, functionalised with anti-*E. coli*), as expected. However, once again, no clear trend in terms of the response of the sensors could be observed. The other parameters extracted from the EIS spectra fittings showed little variation, with the exception of the monotonic increase of the R_s parameter for sample H1. This can be explained by a continuous mechanical deterioration of the electrical contact (silver paint and silver-plated wire).

4. Conclusions and Future Work

The main objective of this work was to develop a biosensing device with graphene as a transducing element, by (1) synthesising, transferring onto a suitable substrate and characterising graphene, by (2) studying and optimising its functionalisation through different strategies and by (3) demonstrating its operation as a biosensing platform.

The first part of this objective was achieved by growing, in a TCVD reactor, graphene samples, which were later identified, using Raman spectroscopy, SEM and optical microscopy, as being single layer graphene with few-layer islands. The transfer of the as-grown samples onto Si/SiO_2 substrates was also optimised in this part. Lastly, the electrochemical performance of the transferred graphene was assessed by EIS and DPV measurements.

To address the second part of the objective, both covalent and non-covalent functionalisations were explored. The covalent one, relying on the hydroxylation of graphene's surface through the Fenton reaction, was unsuccessful, as confirmed by Raman spectroscopy and surface contact angle measurements, despite the various reaction parameters attempted. On the other hand, the success of the non-covalent one, based on the immobilisation of pyrene butyric hydrazide, was evident from the Raman, EIS and XPS spectra. However, no conclusion was reached regarding the optimal functionalisation conditions, as the exact nature of the surface interactions and the resulting changes in the EIS spectra remained unexplained.

The third part of the main objective was addressed by measuring the response of the sensors to different analytes (avidin and hCG). In both cases the sensors' responses were different from the control samples. However, no clearly identifiable biosensing behaviour was observed.

With these results in mind, the following future work is proposed:

- Optimisation of the synthesis process in order to achieve single layer graphene (without any secondary layers). This is important in the context of the non-covalent functionalisation for three reasons. Firstly, given that, due to $\pi - \pi$ interactions, PBH is expected to bond at the basal plane of graphene, any further immobilisations and analyte interactions would only affect the charge transfer at the basal plane. The charge transfer at the secondary layers', however, would remain unaffected, and thus would act as a parasitic parallel signal. Secondly, the contribution of the secondary layers to the charge transfer processes greatly complicates the analysis of the EIS measurements, most likely requiring more complex equivalent circuits than the one used in the present work. Lastly, it's easier to achieve greater reproducibility for single layer graphene than it is for the samples used in this work. This would make any trends in terms of how the different functionalisation parameters affect the electrochemical behaviour of graphene clearer, facilitating optimisation efforts.
- Further exploration of the covalent functionalisation techniques. Here, as mentioned before, the few-layer islands are a feature of interest, and as such this route should be explored in parallel with the previously proposed one.
- Microfabrication of GFETs devices where the functionalisation strategies explored in the present work can be applied. As covered in Section 1.2.2., field effect biosensing offers the opportunity for an extensive exploitation of graphene's unique properties.

References

[1] P. R. Wallace, "The band theory of graphite," *Phys. Rev.*, vol. 71, no. 9, pp. 622–634, 1947.

[2] M. Monthioux *et al.*, "Who should be given the credit for the discovery of carbon nanotubes?," *Carbon N. Y.*, vol. 44, no. 9, pp. 1621–1623, 2006.

[3] H. W. Kroto *et al.*, "C 60: buckminsterfullerene," *Nature*, vol. 318, p. 162, 1985.

[4] N. D. Mermin, "Crystalline Order in Two Dimensions," *Phys. Rev.*, vol. 176, no. 1, pp. 250–254, Dec. 1968.

[5] K. S. Novoselov *et al.*, "Electric field effect in atomically thin carbon films," *Science (80-.).*, vol. 306, pp. 666–669, 2004.

[6] F. Schwierz, "Graphene transistors," *Nat. Nanotechnol.*, vol. 5, no. 7, pp. 487–496, 2010.

[7] X. Huang *et al.*, "Graphene-based composites," *Chem. Soc. Rev.*, vol. 41, no. 2, pp. 666–686, 2012.

[8] H. Jang *et al.*, "Graphene-Based Flexible and Stretchable Electronics," *Adv. Mater.*, vol. 28, no. 22, pp. 4184–4202, 2016.

[9] S. Bae *et al.*, "30 inch Roll-Based Production of High-Quality Graphene Films for Flexible Transparent Electrodes," vol. 5, no. June, pp. 1–5, 2009.

[10] "Graphene Flagship | Graphene Flagship." [Online]. Available: https://graphene-flagship.eu/. [Accessed: 21-Oct-2017].

[11] A. C. Ferrari *et al.*, "Science and technology roadmap for graphene, related two-dimensional crystals, and hybrid systems," *Nanoscale*, vol. 7, no. 11, pp. 4598–4810, 2015.

[12] J. Liu *et al.*, "Graphene and graphene oxide as new nanocarriers for drug delivery applications," *Acta Biomater.*, vol. 9, no. 12, pp. 9243–9257, 2013.

[13] S. Kumar *et al.*, "Comprehensive Review on the Use of Graphene-Based Substrates for Regenerative Medicine and Biomedical Devices," *ACS Appl. Mater. Interfaces*, vol. 8, no. 40, pp. 26431–26457, 2016.

[14] C. I. L. Justino *et al.*, "Graphene based sensors and biosensors," *TrAC - Trends Anal. Chem.*, vol. 91, pp. 53–66, 2017.

[15] S. Kochmann *et al.*, "Graphenes in chemical sensors and biosensors," *TrAC - Trends Anal. Chem.*, vol. 39, pp. 87–113, 2012.

[16] T. Kuila *et al.*, "Recent advances in graphene-based biosensors," *Biosens. Bioelectron.*, vol. 26, no. 12, pp. 4637–4648, 2011.

[17] F. Liu *et al.*, "Graphene-based electrochemical biosensor for pathogenic virus detection," *Biochip J.*, vol. 5, no. 2, pp. 123–128, 2011.

[18] B. Cai *et al.*, "Ultrasensitive label-free detection of PNA-DNA hybridization by reduced graphene oxide field-effect transistor biosensor," *ACS Nano*, vol. 8, no. 3, pp. 2632–2638, 2014.

[19] Y. Chen *et al.*, "Field-Effect Transistor Biosensor for Rapid Detection of Ebola Antigen," *Sci. Rep.*, vol. 7, no. 1, p. 10974, 2017.

[20] S. Teixeira *et al.*, "Epitaxial graphene immunosensor for human chorionic gonadotropin," *Sensors Actuators, B Chem.*, vol. 190, pp. 723–729, 2014.

[21] Y. Liu *et al.*, "Biological and chemical sensors based on graphene materials," *Chem. Soc. Rev.*, vol. 41, no. 6, pp. 2283–2307, 2012.

[22] A. Bianco *et al.*, "All in the graphene family - A recommended nomenclature for two-dimensional carbon materials," *Carbon*, vol. 65. pp. 1–6, 2013.

[23] P. K. Misra, *Physics of Condensed Matter*. Academic Press, 2012.

[24] J. C. Meyer *et al.*, "On the roughness of single- and bi-layer graphene membranes," *Solid State Commun.*, vol. 143, no. 1–2, pp. 101–109, 2007.

[25] K. S. Novoselov *et al.*, "Electronic properties of graphene," *Phys. Status Solidi Basic Res.*, vol. 244, no. 11, pp. 4106–4111, 2007.

[26] K. S. Novoselov *et al.*, “Two-dimensional gas of massless Dirac fermions in graphene.,” *Nature*, vol. 438, no. 7065, pp. 197–200, 2005.
[27] K. I. Bolotin *et al.*, “Ultrahigh electron mobility in suspended graphene,” 2008.
[28] Y. Zhang *et al.*, “Experimental observation of the quantum Hall effect and Berry’s phase in graphene,” *Nature*, vol. 438, no. 7065, pp. 201–204, 2005.
[29] M. I. Katsnelson *et al.*, “Chiral tunneling and the Klein paradox in graphene,” vol. 2, no. September, 2006.
[30] D.-Y. Jeon *et al.*, “Radio-Frequency Electrical Characteristics of Single Layer Graphene,” *Jpn. J. Appl. Phys.*, vol. 48, no. 9, p. 91601, 2009.
[31] Y.-M. Lin *et al.*, “100-GHz transistors from wafer-scale epitaxial graphene,” *Nano*, vol. 327, no. 5966, p. 662, Feb. 2010.
[32] S. Y. Zhou *et al.*, “Substrate-induced bandgap opening in epitaxial graphene.,” *Nat. Mater.*, vol. 6, no. 11, pp. 916–916, 2007.
[33] M. Y. Han *et al.*, “Energy band-gap engineering of graphene nanoribbons,” *Phys. Rev. Lett.*, vol. 98, no. 20, pp. 1–4, 2007.
[34] R. Balog *et al.*, “Bandgap opening in graphene induced by patterned hydrogen adsorption,” *Nat. Mater.*, vol. 9, no. 4, pp. 315–319, 2010.
[35] M. Wilson, “Electrons in atomically thin carbon sheets behave like massless particles,” *Phys. Today*, vol. 59, no. 1, pp. 21–23, 2006.
[36] R. R. Nair *et al.*, “Fine structure constant defines visual transparency of graphene.,” *Science*, vol. 320, no. 5881, p. 1308, Jun. 2008.
[37] A. Kumar *et al.*, “The race to replace tin-doped indium oxide: Which material will win?,” *ACS Nano*, vol. 4, no. 1, pp. 11–14, 2010.
[38] E. Hendry *et al.*, “Coherent nonlinear optical response of graphene,” *Phys. Rev. Lett.*, vol. 105, no. 9, pp. 1–4, 2010.
[39] N. Yoshikawa *et al.*, “High-harmonic generation in graphene enhanced by elliptically polarized light excitation,” *Science (80-.).*, vol. 356, no. 6339, pp. 736–738, 2017.
[40] C. Lee *et al.*, “Measurement of the elastic properties and intrinsic strength of monolayer graphene.,” *Science*, vol. 321, no. 5887, pp. 385–388, Jul. 2008.
[41] I. W. Frank *et al.*, “Mechanical properties of suspended graphene sheets,” *J. Vac. Sci. Technol. B Microelectron. Nanom. Struct.*, vol. 25, no. 6, p. 2558, 2007.
[42] S. Bae *et al.*, “Roll-to-roll production of 30-inch graphene films for transparent electrodes,” *Nat Nano*, vol. 5, no. 8, pp. 574–578, Aug. 2010.
[43] S. Stankovich *et al.*, “Graphene-based composite materials,” *Nature*, vol. 442, no. 7100, pp. 282–286, 2006.
[44] A. A. Balandin *et al.*, “Superior thermal conductivity of single-layer graphene,” *Nano Lett.*, vol. 8, no. 3, pp. 902–907, 2008.
[45] S. Ghosh *et al.*, “Dimensional crossover of thermal transport in few-layer graphene,” *Nat. Mater.*, vol. 9, no. 7, pp. 555–558, 2010.
[46] A. A. Balandin, “Thermal properties of graphene and nanostructured carbon materials.,” *Nat. Mater.*, vol. 10, no. 8, pp. 569–581, Jul. 2011.
[47] W. Cai *et al.*, “Thermal transport in suspended and supported monolayer graphene grown by chemical vapor deposition,” *Nano Lett.*, vol. 10, no. 5, pp. 1645–1651, 2010.
[48] X. Gong *et al.*, “Functionalized-graphene composites: Fabrication and applications in sustainable energy and environment,” *Chem. Mater.*, vol. 28, no. 22, pp. 8082–8118, 2016.
[49] L. S. Walker *et al.*, “Toughening in Graphene Ceramic Composites,” *ACS Nano*, vol. 5, no. 4, pp. 3182–3190, Apr. 2011.
[50] C. Meng *et al.*, “Graphene-doped polymer nanofibers for low-threshold nonlinear optical waveguiding,” *Light Sci. Appl.*, vol. 4, no. 11, p. e348, Nov. 2015.
[51] W. Han *et al.*, “Graphene spintronics,” *Nat. Nanotechnol.*, vol. 9, no. 10, pp. 794–807, Oct.

2014.
[52] S. Kumar *et al.*, “Graphene field emission devices,” *Appl. Phys. Lett.*, vol. 105, no. 10, 2014.
[53] F. Bonaccorso *et al.*, “Graphene photonics and optoelectronics,” *Nat. Photonics*, vol. 4, no. 9, pp. 611–622, Sep. 2010.
[54] F. J. García de Abajo, “Graphene Plasmonics: Challenges and Opportunities,” *ACS Photonics*, vol. 1, no. 3, pp. 135–152, 2014.
[55] X. Wang *et al.*, “Flexible graphene devices related to energy conversion and storage,” *Energy Environ. Sci.*, vol. 8, no. 3, pp. 790–823, 2015.
[56] V. Tozzini *et al.*, “Prospects for hydrogen storage in graphene,” *Phys. Chem. Chem. Phys.*, vol. 15, no. 1, pp. 80–89, 2013.
[57] H. Sevinçli *et al.*, “A bottom-up route to enhance thermoelectric figures of merit in graphene nanoribbons,” *Sci. Rep.*, vol. 3, no. 1, p. 1228, 2013.
[58] Y. Yang *et al.*, “Graphene based materials for biomedical applications,” *Mater. Today*, vol. 16, no. 10, pp. 365–373, 2013.
[59] C. G. Núñez *et al.*, “Energy-Autonomous, Flexible, and Transparent Tactile Skin,” *Adv. Funct. Mater.*, vol. 27, no. 18, p. 1606287, 2017.
[60] X. Zang *et al.*, *Graphene and carbon nanotube (CNT) in MEMS/NEMS applications*, vol. 132. Elsevier, 2015, pp. 192–206.
[61] Q. He *et al.*, “Graphene-based electronic sensors,” *Chem. Sci.*, vol. 3, no. 6, p. 1764, 2012.
[62] M. Jung *et al.*, “Microwave Photodetection in an Ultraclean Suspended Bilayer Graphene p-n Junction,” *Nano Lett.*, vol. 16, no. 11, pp. 6988–6993, 2016.
[63] Y. G. Semenov *et al.*, “Graphene spin capacitor for magnetic field sensing,” *Appl. Phys. Lett.*, vol. 97, no. 1, 2010.
[64] S. H. Bae *et al.*, “Graphene-based transparent strain sensor,” *Carbon N. Y.*, vol. 51, no. 1, pp. 236–242, 2013.
[65] P. Blake *et al.*, “Making graphene visible,” *Appl. Phys. Lett.*, vol. 91, no. 6, p. 63124, 2007.
[66] J. Lee *et al.*, “Scanning electron microscopy characterization of structural features in suspended and non-suspended graphene by customized CVD growth,” *Diam. Relat. Mater.*, vol. 54, pp. 64–73, 2014.
[67] J. C. Meyer *et al.*, “Experimental analysis of charge redistribution due to chemical bonding by high-resolution transmission electron microscopy,” *Nat. Mater.*, vol. 10, no. 3, pp. 209–215, 2011.
[68] C. J. Shearer *et al.*, “Accurate thickness measurement of graphene,” *Nanotechnology*, vol. 27, no. 12, p. 125704, 2016.
[69] J. R. Ferraro *et al.*, *Introductory Raman Spectroscopy*. Academic Press, 2003.
[70] A. C. Ferrari *et al.*, “Raman spectrum of graphene and graphene layers,” *Phys. Rev. Lett.*, vol. 97, no. 18, pp. 1–4, 2006.
[71] M. Hulman, “Raman spectroscopy of graphene,” in *Graphene: Properties, Preparation, Characterisation and Devices*, A. Skakalova, V; Kaiser, Ed. London: Woodhead Publishing Limited, 2014, pp. 156–183.
[72] A. C. Ferrari, “Raman spectroscopy of graphene and graphite: Disorder, electron–phonon coupling, doping and nonadiabatic effects,” *Solid State Commun.*, vol. 143, no. 1, pp. 47–57, 2007.
[73] S. Piscanec *et al.*, “Kohn anomalies and electron-phonon interactions in graphite,” *Phys. Rev. Lett.*, vol. 93, no. 18, pp. 1–4, 2004.
[74] M. S. Dresselhaus *et al.*, “Defect characterization in graphene and carbon nanotubes using Raman spectroscopy,” *Philos. Trans. R. Soc. A Math. Phys. Eng. Sci.*, vol. 368, no. 1932, pp. 5355–5377, 2010.
[75] D. R. Lenski *et al.*, “Raman and optical characterization of multilayer turbostratic graphene grown via chemical vapor deposition,” *J. Appl. Phys.*, vol. 110, no. 1, p. 13720, 2014.

[76] D. Grieshaber *et al.*, "Electrochemical Biosensors -Sensor Principles and Architectures," *Sensors*, vol. 8, no. March, pp. 1400–1458, 2008.
[77] D. R. Thevenot *et al.*, "Electrochemical biosensors: recommended definitions and classification," 2001.
[78] L. C. Clark *et al.*, "Electrode systems for continuous monitoring in cardiovascular surgery," *Ann. N. Y. Acad. Sci.*, vol. 102, no. 1, pp. 29–45, 1962.
[79] V. Scognamiglio *et al.*, "Biosensing technology for sustainable food safety," *Trends in Analytical Chemistry*, vol. 62. pp. 1–10, 2014.
[80] J. D. Newman *et al.*, "Home blood glucose biosensors: a commercial perspective," *Biosens. Bioelectron.*, vol. 20, pp. 2435–2453, 2005.
[81] E.-H. Yoo *et al.*, "Glucose Biosensors: An Overview of Use in Clinical Practice," *Sensors*, vol. 10. pp. 4558–4576, 2010.
[82] J. P. Chambers *et al.*, *Biosensor recognition elements*, vol. 10, no. 1–2. 2008, pp. 1–12.
[83] J. S. Danielsa *et al.*, "Label-Free Impedance Biosensors: Opportunities and Challenges," *Electroanalysis*, vol. 19, no. 12, pp. 1239–1257, 2007.
[84] B. Srinivasan *et al.*, "A Three-Layer Competition-Based Giant Magnetoresistive," pp. 2996–3002, 2011.
[85] D. Issadore *et al.*, "μ Hall Chip for Sensitive Detection of Bacteria," pp. 1224–1228, 2013.
[86] H. J. Hathaway *et al.*, "Detection of breast cancer cells using targeted magnetic nanoparticles and ultra-sensitive magnetic field sensors," pp. 1–13, 2011.
[87] D. Issadore *et al.*, "Ultrasensitive Clinical Enumeration of Rare Cells ex Vivo Using a Micro-Hall Detector," *Sci. Transl. Med.*, vol. 4, no. 141, p. 141ra92, Jul. 2012.
[88] T. A. P. Rocha-Santos, "Sensors and biosensors based on magnetic nanoparticles," *Trends Anal. Chem.*, vol. 62, pp. 28–36, 2014.
[89] P. Damborsky *et al.*, "Optical biosensors," *Essays Biochem.*, vol. 60, pp. 91–100, 2016.
[90] P. Skládal, "Piezoelectric biosensors," *TrAC - Trends Anal. Chem.*, vol. 79, pp. 127–133, 2016.
[91] K. Ramanathan *et al.*, "Principles and applications of thermal biosensors," *Biosens. Bioelectron.*, vol. 16, no. 6, pp. 417–423, 2001.
[92] J. L. Hammond *et al.*, "Electrochemical biosensors and nanobiosensors.," *Essays Biochem.*, vol. 60, no. 1, pp. 69–80, 2016.
[93] M. Santandreu *et al.*, "Determination of β-HCG using amperometric immunosensors based on a conducting immunocomposite," *Anal. Chim. Acta*, vol. 396, no. 2–3, pp. 181–188, 1999.
[94] E. Bakker *et al.*, "Potentiometric sensors for trace-level analysis," *Trends Anal. Chem.*, vol. 24, no. 3, pp. 199–207, 2005.
[95] B. R. Eggins, *Analytical Techniques in the Sciences: Chemical Sensors and Biosensors*. Chichester, UK.: John Wiley & Sons, Ltd., 2002.
[96] J. Janata, *Principles of Chemical Sensors*, 2nd ed. Springer US, 2009.
[97] T. V. Shishkanova *et al.*, "Functionalization of PVC membrane with ss oligonucleotides for a potentiometric biosensor," *Biosens. Bioelectron.*, vol. 22, no. 11, pp. 2712–2717, 2007.
[98] N. Jaffrezic-Renault *et al.*, "Conductometric microbiosensors for environmental monitoring," *Sensors*, vol. 8, no. 4, pp. 2569–2588, 2008.
[99] K. Yagiuda *et al.*, "Development of a conductivity-based immunosensor for sensitive detection of methamphetamine (stimulant drug) in human urine," *Biosens. Bioelectron.*, vol. 11, no. 8, pp. 703–707, 1996.
[100] J. K. Macdonald *et al.*, *Impedance Spectroscopy*. 2005.
[101] A. J. Bard *et al.*, *Electrochemical Methods: Fundamentals and Applications*, 2nd ed. John Wiley & Sons, Inc., 2001.
[102] A. Errachid *et al.*, "FET-based chemical sensor systems fabricated with standard technologies," *Electroanalysis*, vol. 16, no. 22, pp. 1843–1851, 2004.
[103] N. Formisano *et al.*, "Multimodal electrochemical and nanoplasmonic biosensors using

ferrocene-crowned nanoparticles for kinase drug discovery applications," *Electrochem. commun.*, vol. 57, pp. 70–73, 2015.
[104] J. N. Tiwari *et al.*, "Engineered Carbon-Nanomaterial-Based Electrochemical Sensors for Biomolecules," *ACS Nano*, vol. 10, no. 1, pp. 46–80, 2016.
[105] D. O'Hare, "Biosensors and Sensor Systems," in *Body Sensor Networks*, G.-Z. Yang, Ed. London: Springer, 2014.
[106] W. Schuhmann *et al.*, "Miniaturization of biosensors," in *Electrochemical Microsystem Technologies*, J. W. Schultze, T. Osaka, and M. Datta, Eds. CRC Press, 2002, pp. 409–428.
[107] F. Virgilio *et al.*, "Development of electrochemical biosensors by e-beam lithography for medical diagnostics," *Microelectron. Eng.*, vol. 111, pp. 320–324, 2013.
[108] K. T. M. Tran *et al.*, "Lithography-based methods to manufacture biomaterials at small scales," *J. Sci. Adv. Mater. Devices*, vol. 2, no. 1, pp. 1–14, 2016.
[109] D. Falconnet *et al.*, "A combined photolithographic and molecular-assembly approach to produce functional micropatterns for applications in the biosciences," *Adv. Funct. Mater.*, vol. 14, no. 8, pp. 749–756, 2004.
[110] G. Luka *et al.*, "Microfluidics integrated biosensors: A leading technology towards lab-on-A-chip and sensing applications," *Sensors (Switzerland)*, vol. 15, no. 12, pp. 30011–30031, 2015.
[111] D. Mark *et al.*, "Microfluidic lab-on-a-chip platforms: requirements, characteristics and applications," *Chem. Soc. Rev.*, vol. 39, no. 3, p. 1153, 2010.
[112] C. Rivet *et al.*, "Microfluidics for medical diagnostics and biosensors," *Chem. Eng. Sci.*, vol. 66, no. 7, pp. 1490–1507, 2011.
[113] J. Wang, "Nanomaterial-based amplified transduction of biomolecular interactions," *Small*, vol. 1, no. 11, pp. 1036–1043, 2005.
[114] Y. Li *et al.*, "Gold nanoparticle-based biosensors," *Gold Bull.*, vol. 43, no. 1, pp. 29–41, 2010.
[115] B. Willner *et al.*, "Electrical contacting of redox proteins by nanotechnological means," *Curr. Opin. Biotechnol.*, vol. 17, no. 6, pp. 589–596, 2006.
[116] J. M. Pingarrón *et al.*, "Gold nanoparticle-based electrochemical biosensors," *Electrochim. Acta*, vol. 53, no. 19, pp. 5848–5866, 2008.
[117] J. Li *et al.*, "Quantum dots for fluorescent biosensing and bio-imaging applications.," *Analyst*, vol. 138, no. 9, pp. 2506–15, 2013.
[118] W. R. Algar *et al.*, "Beyond labels: A review of the application of quantum dots as integrated components of assays, bioprobes, and biosensors utilizing optical transduction," *Anal. Chim. Acta*, vol. 673, no. 1, pp. 1–25, 2010.
[119] F. Patolsky *et al.*, "Nanowire-based biosensors," *Anal. Chem.*, vol. 78, no. 13, pp. 4260–4269, 2006.
[120] M. Megens *et al.*, "Magnetic biochips: A new option for sensitive diagnostics," *J. Magn. Magn. Mater.*, vol. 293, no. 1, pp. 702–708, 2005.
[121] B. R. Adhikari *et al.*, "Carbon nanomaterials based electrochemical sensors/biosensors for the sensitive detection of pharmaceutical and biological compounds," *Sensors (Switzerland)*, vol. 15, no. 9, pp. 22490–22508, 2015.
[122] Z. Wang *et al.*, "Carbon nanomaterials-based electrochemical biosensors: An overview," *Nanoscale*, vol. 7, no. 15, pp. 6420–6431, 2015.
[123] J. A. Carlisle, "Diamond films: Precious biosensors," *Nat Mater*, vol. 3, no. 10, pp. 668–669, Oct. 2004.
[124] W. Zhang *et al.*, "Nanostructuring of biosensing electrodes with nanodiamonds for antibody immobilization," *ACS Nano*, vol. 8, no. 2, pp. 1419–1428, 2014.
[125] R. N. Goyal *et al.*, "Voltammetric Quantification of Adenine and Guanine at C60 Modified Glassy Carbon Electrodes," *J. Nanosci. Nanotechnol.*, vol. 6, no. 12, pp. 3699–3704, 2006.
[126] V. G. Gavalas *et al.*, "[60]Fullerene-mediated amperometric biosensors," *Anal. Chim. Acta*,

vol. 409, pp. 131–135, 2000.
[127] S. S. Polytechnic, “A Critical Review of Glucose Biosensors Based on Carbon Nanomaterials: Carbon Nanotubes and Graphene,” pp. 5996–6022, 2012.
[128] A. Guiseppi-elie *et al.*, “Direct electron transfer of glucose oxidase on carbon nanotubes,” vol. 559, 2002.
[129] C. Cai *et al.*, “Direct electron transfer and bioelectrocatalysis of hemoglobin at a carbon nanotube electrode,” vol. 325, pp. 285–292, 2004.
[130] J. Kong *et al.*, “Nanotube Molecular Wires as Chemical Sensors,” vol. 287, no. January, pp. 0–3, 2000.
[131] R. J. Chen *et al.*, “Noncovalent functionalization of carbon nanotubes for highly specific electronic biosensors,” vol. 100, no. 9, 2003.
[132] D. A. Heller *et al.*, “Multimodal optical sensing and analyte specificity using single-walled carbon nanotubes,” *Nat. Nanotechnol.*, vol. 4, pp. 114–120, 2009.
[133] S. Chatterjee *et al.*, “Functionalization of carbon buckypaper for the sensitive determination of hydrogen peroxide in human urine,” *Biosens. Bioelectron.*, vol. 35, no. 1, pp. 302–307, 2012.
[134] W. Yang *et al.*, “Carbon Nanomaterials in Biosensors: Should You Use Nanotubes or Graphene?,” *Angew. Chemie Int. Ed.*, vol. 49, pp. 2114–2138, 2010.
[135] M. Pumera, “Carbon Nanotubes Contain Residual Metal Catalyst Nanoparticles even after Washing with Nitric Acid at Elevated Temperature Because These Metal Nanoparticles Are Sheathed by Several Graphene Sheets,” *Langmuir*, vol. 23, no. 11, pp. 6453–6458, 2007.
[136] Y. Lin *et al.*, “Strong Suppression of Electrical Noise in Bilayer Graphene Nanodevices,” 2008.
[137] J. T. Robinson *et al.*, “Reduced Graphene Oxide Molecular Sensors,” 2008.
[138] O. J. Guy *et al.*, “Graphene Functionalization for Biosensor Applications,” in *Silicon Carbide Biotechnology: A Biocompatible Semiconductor for Advanced Biomedical Devices and Applications: Second Edition*, Second Edi., Elsevier Inc., 2016, pp. 85–141.
[139] V. Georgakilas *et al.*, “Functionalization of Graphene: Covalent and Non-Covalent Approaches, Derivatives and Applications,” *Chem. Rev.*, vol. 112, p. 6156−6214, 2012.
[140] M. S. Artiles *et al.*, “Graphene-based hybrid materials and devices for biosensing,” *Adv. Drug Deliv. Rev.*, vol. 63, no. 14–15, pp. 1352–1360, 2011.
[141] S. Pei *et al.*, “The reduction of graphene oxide,” *Carbon N. Y.*, vol. 50, no. 9, pp. 3210–3228, 2012.
[142] G. L. C. Paulus *et al.*, “Covalent electron transfer chemistry of graphene with diazonium salts,” *Acc. Chem. Res.*, vol. 46, no. 1, pp. 160–170, 2013.
[143] S. Eissa *et al.*, “Functionalized CVD monolayer graphene for label-free impedimetric biosensing,” *Nano Res.*, vol. 8, no. 5, pp. 1698–1709, 2015.
[144] J. Liu *et al.*, “Molecularly engineered graphene surfaces for sensing applications: A review,” *Anal. Chim. Acta*, vol. 859, pp. 1–19, 2015.
[145] A. Criado *et al.*, “The Covalent Functionalization of Graphene on Substrates,” *Angew. Chemie - Int. Ed.*, vol. 54, no. 37, pp. 10734–10750, 2015.
[146] V. Georgakilas *et al.*, “Noncovalent Functionalization of Graphene and Graphene Oxide for Energy Materials, Biosensing, Catalytic, and Biomedical Applications,” *Chem. Rev.*, vol. 116, no. 9, pp. 5464–5519, 2016.
[147] R. Forsyth *et al.*, “Graphene Field Effect Transistors for Biomedical Applications: Current Status and Future Prospects,” *Diagnostics*, vol. 7, no. 3, p. 45, 2017.
[148] Y. Ohno *et al.*, “Electrolyte-Gated Graphene Field-Effect Transistors for Detecting pH and Protein Adsorption,” *Nano Lett.*, vol. 9, no. 9, pp. 3318–3322, 2009.
[149] G. Xu *et al.*, “Electrophoretic and field-effect graphene for all-electrical DNA array technology,” *Nat. Commun.*, vol. 5, p. 4866, Sep. 2014.
[150] Y. Huang *et al.*, “Graphene-based biosensors for detection of bacteria and their metabolic

activities," *J. Mater. Chem.*, vol. 21, no. 33, p. 12358, 2011.
[151] L. Zhou *et al.*, "Label-free graphene biosensor targeting cancer molecules based on non-covalent modification," *Biosens. Bioelectron.*, vol. 87, pp. 701–707, Jan. 2017.
[152] A. H. Loo *et al.*, "CVD graphene based immunosensor," *RSC Adv.*, vol. 4, no. 46, pp. 23952–23956, 2014.
[153] K. L. Chavez *et al.*, "A Novel Method of Etching Copper Oxide Using Acetic Acid," *J. Electrochem. Soc.*, vol. 148, no. 11, p. G640, 2001.
[154] R. Muñoz *et al.*, "Review of CVD synthesis of graphene," *Chem. Vap. Depos.*, vol. 19, no. 10–12, pp. 297–322, 2013.
[155] Y. Wang *et al.*, "Electrochemical Delamination of CVD Grown Graphene Film: Toward the Recyclable Use of Copper Catalyst SI," *ACS Nano*, no. 12, pp. 1–10, 2011.
[156] J. W. Suk *et al.*, "Transfer of CVD-grown monolayer graphene onto arbitrary substrates," *ACS Nano*, vol. 5, no. 9, pp. 6916–6924, 2011.
[157] Y. Hiller *et al.*, "Studies on the biotin-binding site of avidin. Minimized fragments that bind biotin.," *Biochem. J.*, vol. 278 (Pt 2, no. OCTOBER, pp. 573–85, 1991.
[158] R. H. Bradley *et al.*, "Surface studies of hydroxylated multi-wall carbon nanotubes," *Appl. Surf. Sci.*, vol. 258, no. 11, pp. 4835–4843, 2012.
[159] K. Barbusiński, "Controversy Over Fenton Mechanism," *Ecol. Chem. Eng. S.*, vol. 16, no. 3, pp. 347–358, 2009.
[160] H. Hiura *et al.*, "Determination of the number of graphene layers: Discrete distribution of the secondary electron intensity stemming from individual graphene layers," *Appl. Phys. Express*, vol. 3, no. 9, 2010.
[161] P. Ramnani *et al.*, "Raman spectra of twisted CVD bilayer graphene," *Carbon N. Y.*, vol. 123, pp. 302–306, 2017.
[162] Z.-J. Wang *et al.*, "Direct Observation of Graphene Growth and Associated Copper Substrate Dynamics by in Situ Scanning Electron Microscopy," *ACS Nano*, vol. 9, no. 2, pp. 1506–1519, 2015.
[163] B. Luo *et al.*, "Copper Oxidation through Nucleation Sites of Chemical Vapor Deposited Graphene," *Chem. Mater.*, vol. 28, no. 11, pp. 3789–3795, 2016.
[164] P. Braeuninger-Weimer *et al.*, "Understanding and Controlling Cu-Catalyzed Graphene Nucleation: The Role of Impurities, Roughness, and Oxygen Scavenging," *Chem. Mater.*, vol. 28, no. 24, pp. 8905–8915, 2016.
[165] I. Vlassiouk *et al.*, "Large scale atmospheric pressure chemical vapor deposition of graphene," *Carbon N. Y.*, vol. 54, pp. 58–67, 2013.
[166] J. Kang *et al.*, "Graphene transfer: key for applications," *Nanoscale*, vol. 4, no. 18, pp. 5527–5537, 2012.
[167] W. Yuan *et al.*, "The edge- and basal-plane-specific electrochemistry of a single-layer graphene sheet," *Sci. Rep.*, vol. 3, p. 2248, Jul. 2013.
[168] F. Mansfeld *et al.*, "Minimization of High-Frequency Phase Shifts in Impedance Measurements," *J. Electrochem. Soc.*, vol. 135, no. 4, p. 906, 1988.
[169] E. Neyens *et al.*, "A Reivew of Classic Fenton's Peroxidaion as an Advanced Technique," *J. Hazard. Mater.*, vol. B98, pp. 33–50, 2003.
[170] M. Hinnemo *et al.*, "On Monolayer Formation of Pyrenebutyric Acid on Graphene," *Langmuir*, vol. 33, no. 15, pp. 3588–3593, 2017.
[171] H. Shinohara *et al.*, "Raman spectra of polycyclic aromatic hydrocarbons. Comparison of calculated raman intensity distributions with observed spectra for naphthalene, anthracene, pyrene, and perylene," *J. Mol. Struct.*, vol. 442, no. 1–3, pp. 221–234, 1998.
[172] V. Venkata Chalapathi *et al.*, "Normal vibrations of N, N-dimethylformamide and N, N-dimethylacetamide," *Proc. Indian Acad. Sci. - Sect. A*, vol. 68, no. 3, pp. 109–122, 1968.
[173] A. Cros *et al.*, "An x-ray photoemission spectroscopy investigation of oxides grown on

AuxSi1-x layers," *J. Appl. Phys.*, vol. 67, no. 4, pp. 1826–1830, 1990.
[174] C. Girardeaux *et al.*, "Analysis of Poly(methyl methacrylate) (PMMA) by XPS," *Surf. Sci. Spectra*, vol. 4, no. 2, pp. 134–137, 1996.
[175] Z. Liu *et al.*, "Synthesis and characterization of hydrazide-linked and amide-linked organic polymers," *ACS Appl. Mater. Interfaces*, vol. 8, no. 46, pp. 32060–32067, 2016.
[176] A. Leung *et al.*, "Synthesis and characterization of alginate/poly-L-ornithine/alginate microcapsules for local immunosuppression," *J. Microencapsul.*, vol. 25, no. 6, pp. 387–398, 2008.
[177] O. C. Compton *et al.*, "Electrically conductive 'alkylated' graphene paper via chemical reduction of amine-functionalized graphene oxide paper," *Adv. Mater.*, vol. 22, no. 8, pp. 892–896, 2010.
[178] M. Yang *et al.*, "One-step photochemical attachment of NHS-terminated monolayers onto silicon surfaces and subsequent functionalization," *Langmuir*, vol. 24, no. 15, pp. 7931–7938, 2008.

Annexes

Table A1 – Summary of the samples used in Section 3.2.

Sample		Characterisation	Functionalisation	Detection Tests
F	**F1**	Raman, Contact Angle	Fenton reaction	-
	F2	Raman, Contact Angle	Fenton reaction	-
A	**A1**	Raman, EIS	Biotin	-
	A2	Raman, EIS	Biotin	-
	A3	Raman, EIS	1 mM PBH, Biotin	-
	A4	Raman, EIS	5 mM PBH, Biotin	-
	A5	Raman, EIS	5 mM PBH, Biotin	-
	A6	Raman	-	-
	A7	Raman	-	-
	A8	Raman	-	-
	A9	Raman	-	-
	A10	EIS	10 mM PBH	Avidin
	A11	EIS	10 mM PBH, Biotin	Avidin
	A12	EIS	10 mM PBH, Biotin	Avidin
	A13	EIS	25 mM PBH, Biotin	Avidin
	A14	EIS	10 mM PBH	Avidin
	A15	EIS	25 mM PBH, Biotin	Avidin
	A16	EIS, XPS	10 mM PBH	-
	A17	EIS, XPS	10 mM PBH, Biotin	-
H	**H1**	EIS	10 mM PBH, anti-E. coli	hCG
	H2	EIS	10 mM PBH, anti-hCG	hCG
	H3	EIS	25 mM PBH, anti-hCG	hCG